PLASMON—DAMPING CHEMICAL SENSOR FOR HYDROGEN FUEL MONITORING

By

RAMA KRISHNA RAO GOWD EDE

Bachelor of Technology in Mechanical Engineering

Acharya Nagarjuna University

Guntur, Andhra Pradesh

2005

Submitted to the Faculty of the
Graduate College of the
Oklahoma State University
in partial fulfillment of
the requirements for
the Degree of
MASTER OF SCIENCE
December, 2011

PLASMON—DAMPING CHEMICAL SENSOR FOR HYDROGEN FUEL MONITORING

Thesis Approved:

Dr. A. Kaan Kalkan, Assistant Professor of Mechanical
and Aerospace Engineering
Thesis Adviser

Dr. Sandip P. Harimkar, Assistant Professor of
Mechanical and Aerospace Engineering
Committee Member

Dr. Kevin Ausman, Assistant Professor of Chemistry
Committee Member

Dr. Sheryl A. Tucker
Dean of the Graduate College

TABLE OF CONTENTS

LIST OF FIGURES

Figure **Page**

Figure **Page**

CHAPTER I

INTRODUCTION

1.1 Motivation

Fossil fuels meet more than 70% of the world's energy demand. It is estimated that energy demand will increase by 50% by 2030. On the other hand, future reliance on the fossil fuels is an uncertainty due to the depletion of this natural resource. In addition, combustion of fossil fuels produces harmful emissions with co-production of greenhouse gases. Therefore, to address these increasing concerns, there is an indispensable demand for clean, alternative, and sustainable energy approaches more than ever before. Hydrogen molecule (H_2) is the smallest carrier of chemical energy that exhibits the highest energy content per unit mass (120 KJ/g) among all chemical fuels [1]. This energy content is 2.5 times higher than the gasoline's widely used petroleum product. Unlike gasoline and diesel, burning of hydrogen fuel yields essentially pure water leading to no greenhouse gas and particulate emissions [2]. Fuel cells (FCs) can utilize H_2 and convert it to electric energy at 80% efficiency. For these reasons, hydrogen based FCs are emerging technology with applications in automobiles, remote appliances, and all possible power generation units [3].

1.2 Fuel cells and their basics

The invention of the fuel cell is credited to Sir William Robert Grove (1908). FCs are electrochemical cells that convert chemical energy of a fuel, such as methanol and hydrogen into electric energy. In the case of conventional electrochemical cells such as batteries, the lifetime of the cells is limited due to the limited amount of fuel (anode). On the other hand, FCs theoretically have unlimited lifetime because of the unlimited supply of fuel from an external source. In addition, FCs consist of no movable mechanical parts leading to low noise and maintenance.

A fuel cell typically comprises of an anode and a cathode that are separated by an electrolyte. The current available FCs are classified on the basis of the employed electrolyte such as phosphoric acid fuel cells (PAFC), proton exchange membrane (PEM) fuel cells, molten carbonate fuel cells (MCFC), solid oxide fuel cells (SOFC), and alkaline fuel cells (AFC). In addition to being quiet and having low-weight, PEM fuel cells especially have gained a significant interest due to the following advantages. First, they require comparatively low operating temperature (80 ^{o}C). Second, they show a higher power-density than the other FCs. These attractive features of the PEM can be exploited in light-duty transportation [3].

Figure 1 illustrates the basics of a PEM fuel cell and its half-cell electrochemical reactions. Hydrogen fuel is supplied at the anode where a transition metal catalyst (Ni or Pt) is employed to dissociate H_2 into protons and electrons (oxidation). Subsequently, the dissociated protons diffuse towards the cathode through the solid polymer electrolyte.

Concomitantly, the electrons released at the anode are conducted towards the cathode, where they are used by the reduction reaction. Water is generated at the cathode from the reaction of the protons with oxygen (O_2) and conducted electrons, which are available at the cathode. The total voltage (electromotive force, emf) generated in the cell is equal to the sum of the oxidation and reduction half-cell voltages.

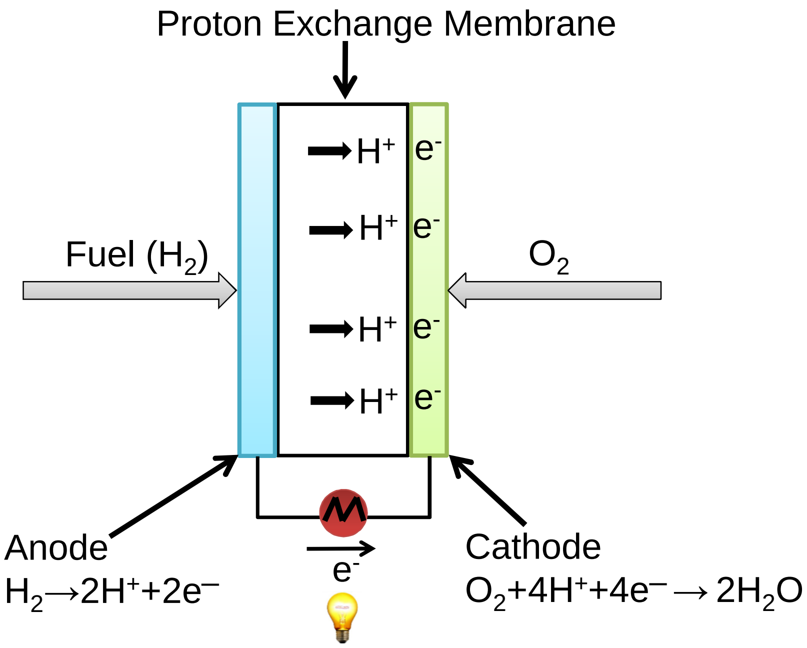

Figure 1: Schematic of the PEM fuel cell illustrating the oxidation and the reduction reactions at the anode and cathode, respectively.

1.3 Degradation of fuel cells performance

Despite all the advantages of the FCs, a crucial drawback is that their use is limited by transition-metal catalyst poisoning with impurities, such as H_2S, NH_3, and CO, present in the hydrogen fuel. In the United States, 95 percent of hydrogen is produced by steam reforming of natural gas (methane) [2]. Hydrogen is also obtained by coal gasification and bio-fuels. Even after the widely used purification process known as desulfurization, the produced hydrogen fuel still contains sulfur compounds, such as SO_2 and H_2S.

Hydrogen sulfide (H_2S) has a high affinity to the transition metals like nickel (Ni) and platinum (Pt). It chemisorbs to the metal catalyst and blocks adsorption of the hydrogen molecule. This situation has a negative effect on the performance of the fuel cell. The performance of the fuel cell degrades irreversibly in the presence of ppb levels of hydrogen sulfide (H_2S) in the hydrogen fuel. Polarization studies have revealed that the performance of the fuel cell was considerably degraded after 4 hours of exposure to 1 ppm concentration of H_2S [4, 5]. The same studies have also shown that the cell was completely degraded within 21 hours of operation due to H_2S chemisorption. Although there are several commercial sulfur sensors available in the market currently, their sensitivity is limited to high ppm levels indicating that there is a vital need for development of ppb level H_2S sensors for monitoring the quality of hydrogen fuel for FC use.

1.4 Objectives and approach of this thesis

The major objective of the present work is to develop a novel plasmon-damping based H_2S sensor for the monitoring of hydrogen fuels utilized in FCs. The active component of the current sensor is a monolayer of silver (Ag) nanoparticles (NPs) immobilized on a Si substrate. The specific objectives of this work are listed as follows:

- To detect ppb levels of sulfur impurities in H_2 using sensitive novel mechanism: adsorbate-induced damping of hybrid plasmon-resonance, associated with Ag nanostructures. This aim involves a unique and simple electroless reduction technique for the synthesis of closely spaced Ag NPs on Si film that leads to hybrid plasmon modes.

- To relate time rate of plasmon-damping change to H_2S concentration.
- To integrate the nanosensor with a hand-held, portable, and miniature spectrophotometer.
- To have a sensitivity of 100 ppb and response time of less than a minute.

Because of their small size, NPs show interesting and different optical properties from those in the bulk. For example, considerably small Ag and Au NPs show intense colors. These intense colors are displayed by the NPs, because they absorb and scatter light intensively in the visible region. Sum of absorption and scattering is called as extinction (absorption + scattering). This extinction is primarily attributed to the resonant coupling of light with the collective electron oscillations of the NPs, namely the localized surface plasmon (LSP) modes [6]. LSP can be driven resonantly at a specific frequency known as localized surface plasmon resonance (LSPR) frequency.

When excited by light, the oscillating electric field causes a displacement of the electron gas of a metal nanoparticle. However, this displaced electron gas is restored back to equilibrium position by the Columbic forces applied by the nanoparticle's positively charged atomic cores. This collective oscillation of electron gas is called as plasmon. The whole restoring force situation can conceivably be treated as a spring-mass system that is resonantly excited with an oscillating electromagnetic (EM) field as the driving force. Its related natural frequency represents the LSPR frequency. The position of this frequency is subjected to spectral shifts when dielectric medium (molecular adsorbates) surrounding the NP undergoes a change. When molecules adsorb on the particle, they decrease the restoring force of the collective oscillation of the NP electron gas. This leads to a decrease in the resonance frequency, thus causing a red shift in the EM spectrum. This spectral shift has often been exploited as the detection principle for a variety of LSPR refractive index sensors [7-12]. Traditionally, these sensors are accomplished by chemically modifying the NP surface with surface active agents or surfactants, which show a high affinity to the analyte.

Alternatively, the present work investigates a novel sensing mechanism associated with the nanoparticles called plasmon-damping as a probe to detect molecular adsorbates. Plasmon-damping is analogous to viscous damping (friction) where the collective oscillation of the electron gas (plasmon) is dampened by an attached dash post (molecular adsorbates). The degree of this plasmon-damping can be measured by a simple UV-visible spectrometer as explained in Section 2.5. In this work, sulfur adsorbates are anticipated to distort the local electric potential at the nanoparticle surface leading to increased electron scattering causing increased plasmon-damping [13]. In addition, sulfur adsorbates induce localized quantum states on the Ag surface. These induced quantum states will assist charge transfer at the interface due to alignment of their surface energy states leading to a dephasing of plasmon. This special type of damping is often referred to as chemical interface damping (CID) [14]. Therefore, plasmon-damping associated with the present Ag NPs may undergo a significant change upon the adsorption of sulfur molecules even in ppb level, thereby providing a highly sensitive sulfur sensing mechanism.

The present work employs a unique electroless reduction technique for the synthesis of Ag NPs on Si substrate [15]. The significance of this reduction technique is its ability to provide well-supported and closely spaced (nm) Ag NPs as shown by the AFM image of Fig. 4.1 (Section 4.1). These unique features are attained due to the following reasons: Since the Fermi level of Ag is at higher energy compared to the underlying amorphous silicon film (a-Si), an electron transfer occurs from Ag NPs to Si to attain thermodynamic equilibrium. This charge transfer causes Ag NPs to acquire a positive charge (+) and Si a negative charge (—). Hence, immobilization occurs by Coulombic attraction due to opposite charges. In addition, during the electroless synthesis, the increase in the positive charge of NP with growth induces an increase in the NP potential. Once these positively charged Ag NPs reach a certain potential, the Ag^+ ions of the electroless solution are repelled by the identically charged Ag NPs. As a consequence, the increase in the NP potential reduces the Ag reduction potential and stops the reaction [16]. Thus, the increase in the NP positive charge developed during the electroless reduction self-inhibits Ag NPs growth, preventing the particle aggregation despite close interparticle (nm) spacing. Such closely separated nanoparticles aid hybrid plasmon mode in addition to the regular LSP mode. This kind of hybrid mode is induced by the strong EM interactions of individual regular LSP modes which offers superior sensitivity compared to any other LSPR sensing mechanisms.

Finally, different concentrations of H_2S (225 ppb, 120 ppb, and 65 ppb) used in this work are obtained by mixing H_2S in pure H_2 using mass flow controllers. Then these concentrations are exposed to the Ag NPs at a fixed flow rate (520 sccm). The presence of flow allowed the present sensor to detect trace levels of H_2S adsorbates with a significant reduction in the response time.

1.5 Significance of the present research

The significance and novel features of the present research is discussed below:

- The present work is unique in considering a novel sensing mechanism, hybrid plasmon-damping, for chemical sensing as an alternative to LSPR based refractive index sensors. This hybrid plasmon-damping, which is associated with the Ag NPs, shows a superior sensitivity even to ppb levels of sulfur impurities. Thus, the present technique provides a highly sensitive sulfur sensor, in particular for FC applications.
- The present sensing component (Ag NPs on Si film) is fabricated by employing an innovative electroless reduction technique. Unlike conventional fabrication techniques, such as colloidal and lithography [17-19], the present reduction technique does not require any surfactants for controlling the size and aggregation of nanoparticles. Generally, these surfactants block the nanoparticle surface from interacting with analyte, thus reducing the sensitivity and response time of the sensor. Therefore, the absence of such surfactants offer a substantial increase in the sensitivity and response time due to direct exposure of the nanoparticle surface with sulfur.
- The strong chemical affinity between the Ag and sulfur also contributes to the sensitivity of the present sensor.

- The present sensing mechanism (i.e., plasmon-damping) can easily be measured by a simple UV-visible spectrophotometer. The tiny probe size (2 mm) of the UV-visible spectrophotometer allows the sensor to have a smaller foot print. Hence, this compact feature enables the present sensor to be low cost, light weight, and portable.
- In the present work, the steady state diffusion adsorption is circumvented with the forced convective flow approach. This flow approach reduces the sensor response time profoundly from minutes to a few seconds.

1.6 Organization of the thesis

The present thesis is organized as follows. Chapter 2 provides the background relating to optical properties of the nanoparticles, plasmon-damping, and current sulfur sensing mechanisms. Chapter 3 elaborates the experimental methods and characterization techniques that are employed in the present thesis. Chapter 4 discusses key findings pertaining to the experimental results with an emphasis on the plasmon-damping kinetics. Finally, Chapter 5 draws the important conclusions from the present thesis.

CHAPTER II

BACKGROUND

2.1 Localized surface plasmon resonance

A plasmon is defined as the collective oscillation of the electron gas in a metal nanoparticle (NP). This plasmon can be considered as a spring-mass system where light (oscillating EM field) acts as a driving force to collectively displace the electron gas with respect to the fixed atomic cores, which are positively charged. Localized surface plasmon (LSP) is an optical phenomenon which occurs when light couples with the plasmon in a metal NP, provided the size (R) of the NP is comparable to the wavelength of the excited light. LSP undergoes resonance at a specific excitation frequency, known as localized surface plasmon resonance (LSPR) frequency. The natural frequency of the spring-mass system which corresponds to LSPR frequency (ω_o) is given by:

$$\omega_o = \sqrt{\frac{K}{m}} \qquad (2.1)$$

where, K is the force constant and m is the mass of the electron gas that is contributing to the plasmon. The LSPR phenomenon and its corresponding resonantly excited spring mass system are illustrated in Fig. 2.1.

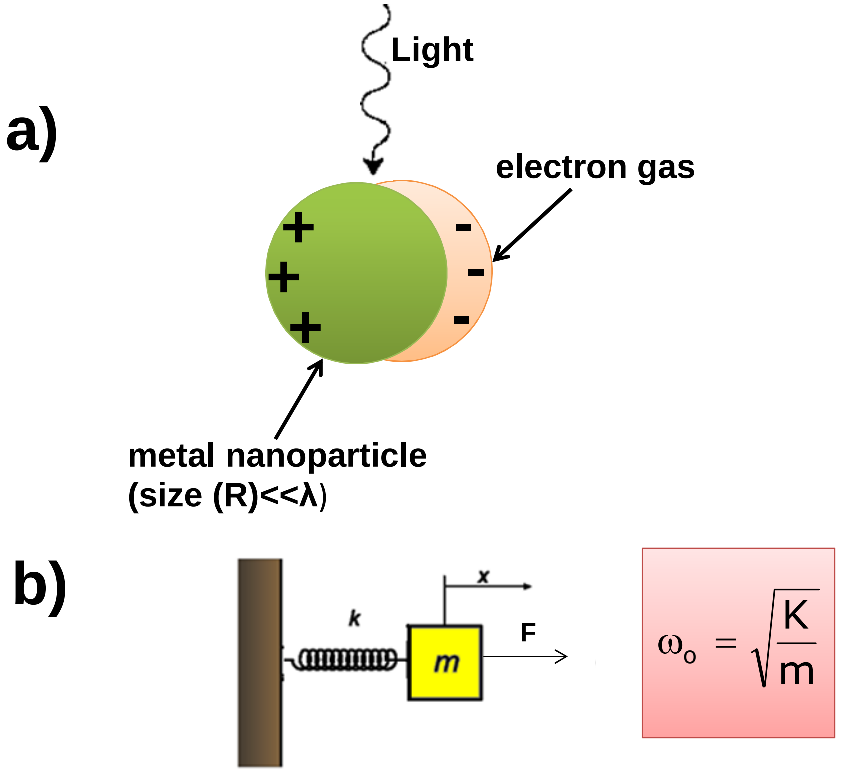

Figure 2.1: Schematic showing the collective oscillation of electron gas of the NP under the action of light (a) and its analogous harmonic oscillator model (b).

For noble metal nanoparticles (NMPs), such as Ag and Au, the LSPR frequency lies in visible region of the EM spectrum. In the case of NPs of size 20 nm, Au NPs exhibit LSPR frequency in green region (520 nm) and Ag NPs in blue region (400 nm) [20]. These visible LSPR frequencies of Ag and Au are responsible for intense colors displayed by medieval arts and pottery [21]. Figure 2.2 displays the 4th century AD Lycurgus cup, which is currently located at British museum, London. The presence of colloidal Au NPs is responsible for the ruby red color that is exhibited when light is transmitted from inside the glass cup [22].

Figure 2.2: 4th century AD Lycurgus cup which looks ruby red due to the presence of colloidal gold NPs.

However, the fundamental understanding of these bright colors remained unclear for centuries. In 1857, Michael Faraday explained the origin of these bright colors by an ordered study of colloidal Au NPs with different sizes [23]. Later, in 1908 Gustav Mie explained the color formation by an analytical solution of the Maxwell's equations [24]. Studies have shown that the LSPR is subjected to spectral shifts when NPs undergo change in size, shape, and surrounding dielectric medium [25-27]. A detailed explanation of all these effects on the plasmon resonance was elegantly reported and reviewed by Krebig and Vollmer [6]. Because of their tunable optical properties, NMPs have received great attention in the view of fundamental understanding as well as for the applications in biological and chemical sensing.

2.2 Plasmon hybridization

Plasmon hybridization arises due to the strong electromagnetic (EM) interaction between adjacent plasmonic oscillators. Hybridization phenomenon is analogous to molecular orbital theory where bonding and antibonding energy levels are formed when two metal NPs approach one another [28]. The EM interaction develops two hybrid modes replacing the regular plasmon mode. In the bonding case, the dipoles of the two adjacent NPs align with each other causing the LSPR frequency of the hybrid mode to occupy lower energy level. The frequency of the bright hybrid plasmon mode can be shifted to further low energy simply by decreasing the interparticle distance [29]. This energy shift is found to be a function of the interparticle distance (S) scaled by the NP size (R) as: $(S/R+1)^{-3}$ [30]. Whereas, in the antibonding case, the opposite dipoles cancel each other therefore hybrid modes associated with this case cannot be excited. In recent years, hybridization is an emerging field of study because these modes can be significantly altered by the molecular adsorption [31, 32]. Figure 2.3 illustrates the plasmon hybridization phenomenon and the effect of interparticle distance or gap width on the hybrid mode position.

2.3 Plasmon—damping

Plasmon is a short-lived quasi particle with a lifetime of ~5 fs [33]. The plasmon decay or damping can be either non-radiative (heat generation via absorption) or radiative (scattering of photons). Non-radiative damping is caused by scattering of electrons by phonons, lattice imperfections including the ones at the NP surface, and impurities [6].

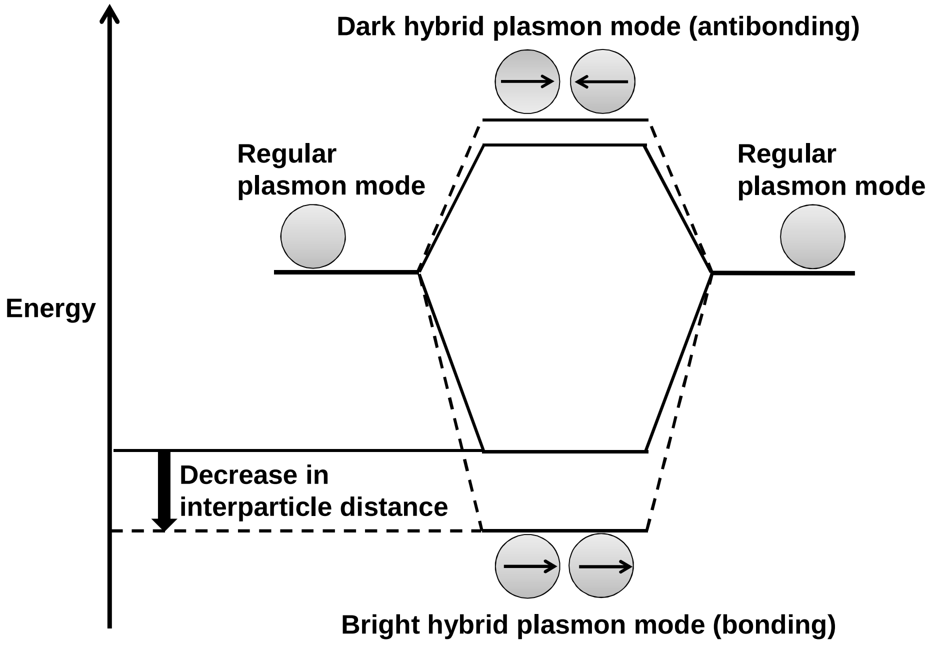

Figure 2.3: Plasmon hybridization of two closely spaced NPs showing the development of hybrid plasmon modes. The low energy shift of the bright hybrid plasmon frequency occurs with decreasing interparticle distance between the NPs.

Following the Mathiessen rule, non-radiative damping due to abovementioned bulk effects can be written as:

$$\Gamma_{\mathrm{bulk}} = \Gamma_{\mathrm{e-e}} + \Gamma_{\mathrm{e-phonon}} + \Gamma_{\mathrm{dislocations}} + \Gamma_{\mathrm{grainboundaries}} + \Gamma_{\mathrm{point\,defects}} \qquad (2.2)$$

The above effects can be lumped to electric resistivity as:

$$\Gamma_{\mathrm{bulk}} = \frac{\rho \cdot n \cdot e^2}{m_e} \qquad (2.3)$$

In the above equation, ρ is the electrical resistivity, n is the electron density, e is the electron charge, and m_e is the effective mass of electrons. Based upon the bulk conductivity (Equation 2.3), the theoretical damping of Ag is 0.017 eV.

The above mentioned Γ_{bulk} in Equation 2.2 should be a constant since the scattering events are largely dominated by electron-phonon term. However, in the case of NP with a size (R) much smaller than the electron mean free path length (~50 nm for Ag [34]), the contribution of the electron scattering at the surface plays an important role. Thus, an additional non-radiative damping term is incorporated to the existing Γ_{bulk} as [35]:

$$\Gamma_{nonrad} = \Gamma_{bulk} + \frac{A \cdot \nu_f}{R} \qquad (2.4)$$

where, A is the shape factor, ν_f the Fermi velocity of the electrons, and R is the NP size, which is comparably smaller than the electron mean free path length.

On the other hand, if size of the NP increases (>30 nm for Ag [6]) then the plasmon decay occurs by the radiative damping. As the volume of the NP increases, plasmon becomes out of phase with the incident electric field, causing the plasmon to collapse. The radiative plasmon-damping (Γ_{rad}) as a function of volume (V) is given as [36]:

$$\Gamma_{rad} = \frac{h \cdot k \cdot V}{\pi} \qquad (2.5)$$

Here, h is the Planck's constant and k is the radiation-damping proportionality constant. Therefore, the total damping (Γ_{Total}) that constitutes both non-radiative and radiative damping pathways can be expressed as:

$$\Gamma_{\text{Total}} = \Gamma_{\text{nonrad}} + \Gamma_{\text{rad}} = \Gamma_{\text{bulk}} + \frac{A \cdot \nu_f}{R} + \frac{h \cdot k \cdot V}{\pi} \qquad (2.6)$$

In the present thesis, the average size of the Ag NP is found to be 36 nm. Therefore, plasmon-damping is subjected to both radiative and non-radiative decay mechanisms. This plasmon-damping can be extracted from the extinction spectrum recorded by a spectrophotometer as explained in Section 2.5.

2.4 Adsorbate—induced damping

When a molecule adsorbs to the NP surface, two additional nonradiative damping processes contribute towards the plasmon-damping. The first process is chemical interface damping (CID) or dynamic charge transfer [37]. In CID, valence electrons of the adsorbed molecules induce well-resolved energy states near the Fermi level of the NP. Although, electron access to these surface energy states require the surmounting of an activation barrier, conduction electrons of the NP can leak into the surface energy states of the adsorbed molecules by quantum mechanical tunneling. After staying a while in the surface energy states of the molecule, the leaked electrons can tunnel back to the Fermi level of the NP. These tunneled back electrons are out of phase with the existing plasmon and cause the plasmon to collapse. The second damping process is due to electron-surface perturbations by molecular adsorbates [6, 13]. When adsorbed on the

NP surface, the molecules change the surface potential of the NP. This change in surface potential also contributes to the plasmon decay by electron scattering. Therefore, the total adsorbate-induced damping is given as:

$$\Gamma_{\mathrm{adsorbates}} = \Gamma_{\mathrm{CID}} + \Gamma_{\mathrm{surface}} \qquad (2.7)$$

In the present hybrid plasmon-damping sensor study, when sulfur molecules adsorb on the Ag NPs, the plasmon is subjected to both CID and electron-surface damping. Different pathways that contribute to the plasmon-damping as discussed earlier are illustrated in Fig. 2.4.

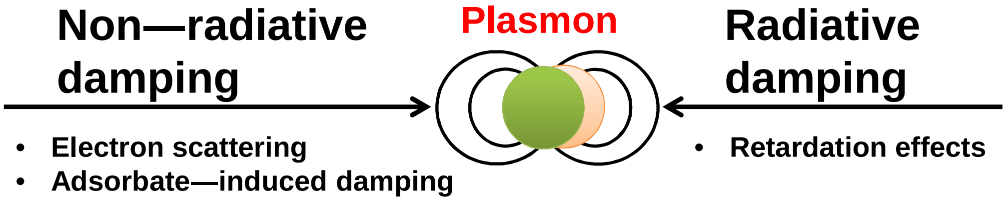

Figure 2.4: Schematic showing the plasmon decay mechanisms in different pathways. These pathways include non-radiative and radiative damping.

2.5 Optical extinction spectroscopy

In a medium composing of NPs, intensity of the incident light beam is attenuated by two mechanisms: absorption and scattering. Absorption occurs when excited electrons in the NP emit phonon. On the other hand, scattering occurs when the excited electrons radiate photons. Extinction is the sum of the absorption and scattering. When light propagates through the particles, part of the light is absorbed and scattered, while the remnant reaches detector. Hence, the transmitted light detected by the detector characterizes the amount of light intensity attenuated via extinction. Figure 2.5 shows the extinction measurement of the NPs by employing a spectrophotometer.

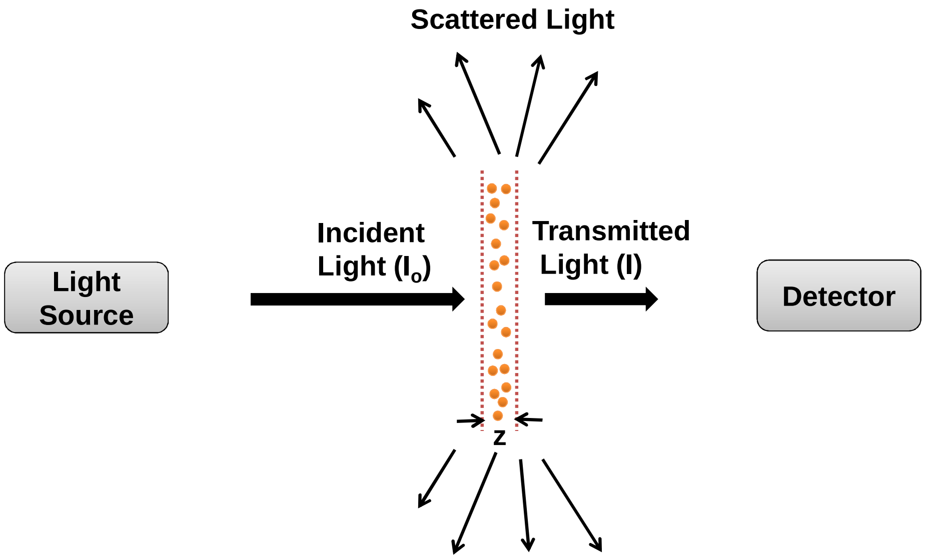

Figure 2.5: Sketch illustrating the extinction by NPs and its characterization using photo-spectrometer.

In optical spectroscopy, relation between the extinction and the transmission (T) is given by:

$$\text{Extinction} = -\log(T) \qquad (2.8)$$

In the above expression, T is defined by I/I_0. According to Beer-Lambert's relation, T is given by:

$$T = \frac{I}{I_0} = 10^{-k \cdot z} \qquad (2.9)$$

where, I is the intensity of the light beam transmitted through the thickness z of NP medium and I_0 is the intensity of the incident beam. k is the extinction coefficient which quantifies how intense the NPs absorbs + scatters the light, and it is defined as:

$$k = n \cdot \sigma_{ext} \qquad (2.10)$$

where, n is the NP density, σ_{ext} is the extinction cross section of a single NP (i.e., area that is effectively influenced by the stream of photons during the extinction). Therefore, extinction cross section constituting both absorption and scattering can be written as:

$$\sigma_{ext} = \sigma_{abs} + \sigma_{sca} \qquad (2.11)$$

Here, σ_{abs} denotes the absorption cross section and σ_{sca} is the scattering cross section of the single NP, respectively.

If the size of metal NP is much smaller than wavelength of the incident light (< 20 nm), then the extinction cross section is significantly contributed by the regular dipolar mode. Mie equation for the extinction cross section corresponding to regular dipolar mode is given as [25]:

$$\sigma_{ext} = \frac{9 \cdot v_o \cdot \varepsilon_m{}^{3/2}}{c} \cdot \left(\frac{\omega \cdot \varepsilon_2(\omega)}{[\varepsilon_1(\omega) + 2 \cdot \varepsilon_m]^2 + \varepsilon_2(\omega)^2} \right) \qquad (2.12)$$

where, ω is the angular frequency of the incident light, v_o represents volume of the particle, c is the light velocity, $\varepsilon(\omega) = \varepsilon_1(\omega) + i\varepsilon_2(\omega)$ denotes the dielectric function of the particle material, and ε_m is the dielectric constant of the surrounding medium.

From the simplified free electron theory, the real and complex dielectric functions can be written as [6]:

$$\varepsilon_1(\omega) = 1 - \frac{\omega_p{}^2}{\omega^2} \qquad (2.13)$$

and

$$\varepsilon_2(\omega) = \frac{\omega_p{}^2 \cdot \Gamma}{\omega^3} \qquad (2.14)$$

Here, ω_p is the bulk plasma frequency (9.08 eV for Ag [38]) and Γ is the phenomenological damping (i.e, $\Gamma << \omega$). By substituting $\varepsilon_1(\omega)$ and $\varepsilon_2(\omega)$ in Equation 2.12, the extinction cross section further reduces to Lorentzian form as below:

$$\sigma_{ext} = \frac{3}{4} \cdot \frac{v_o}{c} \cdot \frac{\varepsilon_m{}^{3/2}}{(1 + 2 \cdot \varepsilon_m)} \cdot \frac{\omega_o{}^2 \cdot \Gamma}{(\omega - \omega_o)^2 + (\Gamma/2)^2} \qquad (2.15)$$

Extinction in the above equation shows resonance at $\omega = \omega_o$, where ω_o denotes extinction maximum or the LSPR frequency.

Figure 2.6 depicts an example extinction spectrum of the NPs. The middle region of the spectrum represents the plasmon resonance peak. For a single NP, the extinction peak exhibits a Lorentzian line shape. This Lorentzian type peak reports the extinction maximum, extinction height, and full width at half maximum (FWHM) or damping factor (Γ). Damping factor (Γ) is a significant parameter in the present study.

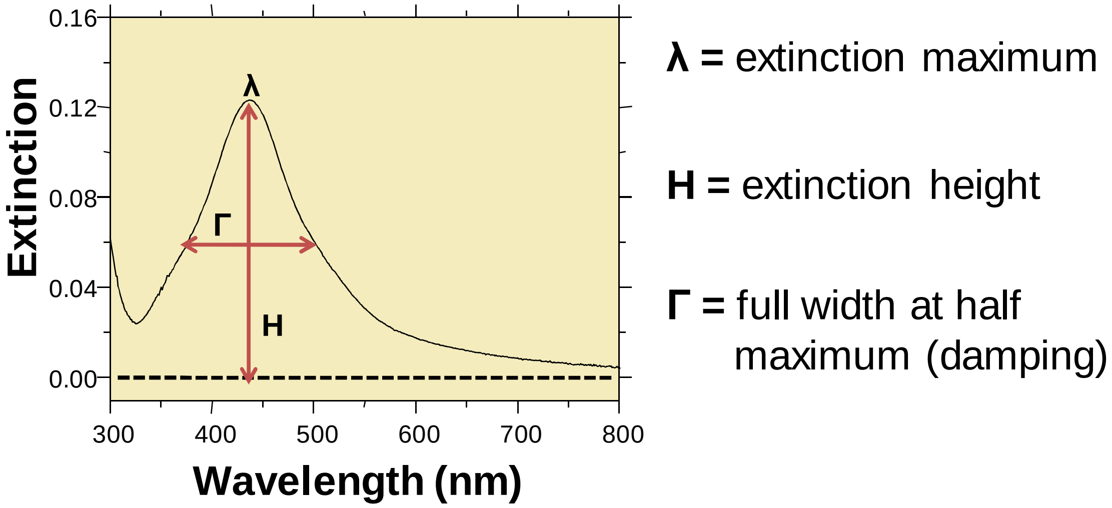

Figure 2.6: UV-visible spectrophotometer recorded extinction spectrum of the NPs and its associated extinction parameters.

It is noteworthy to mention that the above resonance peak is commonly subjected to homogeneous broadening (i.e., Lorentzian). While in ensemble measurements, the effect of distribution of particle's size, shape, and interparticle distance is to cause heterogeneous broadening of the resonance peak. In the present study, Ag NPs are employed because of their ability to show extinction peak in the visible region. Hence, their extinction can easily be detected with a conventional UV-visible spectrophotometer. Also, the low damping of Ag compared to other metal NPs can characterize the change in plasmon-damping more effectively which is crucial for sensing [39].

2.6 Effect of dielectric environment on LSPR

As discussed earlier, the LSPR is subjected to spectral shifts when NPs undergo a change in the dielectric environment. This effect is the most extensively explored LSPR sensing mechanism until now. To illustrate this phenomenon, let us consider the Mie equation. From Equation 2.12, extinction cross section shows maximum value at:

$$\varepsilon_1(\omega) = -2 \cdot \varepsilon_m \qquad (2.16)$$

This is known as resonance condition and its dependency on the dielectric function of the medium surrounding the NP is the basis for refractive index based LSPR sensors [40]. By using the relation of $\varepsilon_1(\omega)$ expressed in terms of wavelengths (Equation 2.13) and dielectric constant expressed as the index of refraction (i.e., $\varepsilon_m = n_m{}^2$), Equation 2.16 reduces to a form as:

$$\lambda_{max} = \lambda_p \sqrt{2 \cdot n_m{}^2 + 1} \qquad (2.17)$$

where, λ_{max} is the LSPR peak position in nm and λ_p is the bulk plasma frequency. Hence, LSPR peak wavelength shows a linear dependence on the refractive index (n) of the medium as shown in Fig. 2.7 (λ_p is considered as 236 nm and n_m range is chosen appropriately).

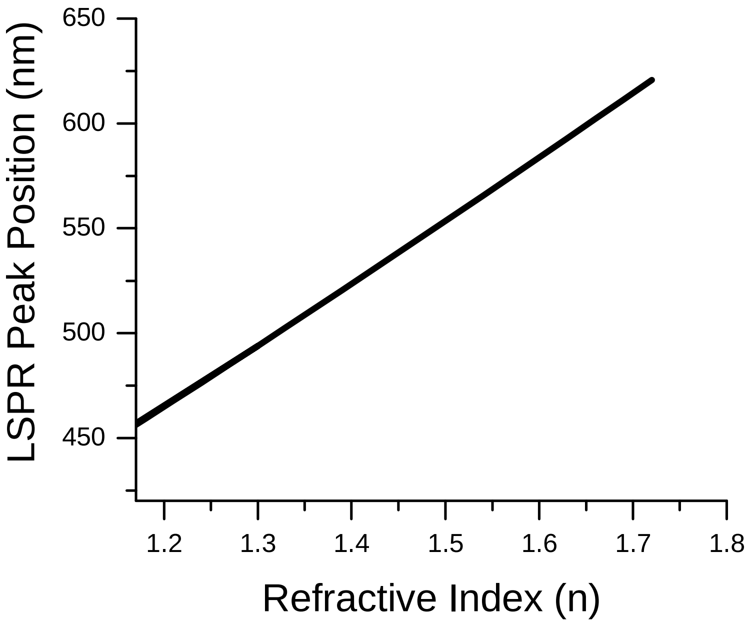

Figure 2.7: Drude model derived LSPR peak wavelength linear dependence on the refractive index (RI).

Previously, several groups have already exploited this refractive index sensing mechanism by measuring the change in 'n' when bulky biomolecules are attached on the NP surface [7-12, 40]. However, LSPR gas sensors are less exploited due to the insignificant refractive index change showed by the attachment of small gas molecules. Recently, Van Duyne et al. employed high resolution LSPR spectroscopy to circumvent this drawback. They reported two separate gas nanosensors using the same RI principle. In the first sensor, they produced Ag plasmonic nanostructures functionalized with Cu acetate and benzenetricarboxylate acid to monitor pure CO_2 and SF_6 gases. Using these nanostructures, they measured the LSPR shift (i.e., $\Delta\lambda_{\text{max}} = \lambda_{\text{test gas}} - \lambda_{N_2}$) for CO_2 and SF_6 gas exposures as 0.13 nm and 0.17 nm, respectively [41]. In the second sensor, they have reported Ag and Au nanoparticles fabricated by nanosphere lithography that can detect miniature changes $(< 3\times10^{-4})$ in bulk refractive index (n) when the gas environment was altered from He to either Ar or N_2 using LSPR spectroscopy [42]. More recently, Mayer and Hafner reviewed the use of plasmonic materials for LSPR refractive index based gas sensors [43]. They explained the critical factors that can influence the sensor performance, such as structure effect on LSPR spectral shift sensitivity. Also, they addressed the LSPR sensor response issues related to the chemical modification of the NPs explicitly.

In opposite to the RI sensing mechanism, the chemical sensor studied in the present thesis use plasmon-damping as a sensing mechanism. To the best of our knowledge, LSPR sensors based on the plasmon-damping mechanism are not yet been reported. Thus, the present study is unique on its own and contributes significantly in the development of highly sensitive LSPR based chemical sensors.

2.7 Current H_2S sensor technologies

The existing sensors that are currently used to detect H_2S include gas chromatography (GC) coupled with detectors, such as flame photometric detector (FPD), pulsed flame photometric detector (PFPD), and sulfur chemiluminescence detector (SCD). Other notable technologies that are widely used for detection of H_2S gas in low concentrations include solid state sensors, electrochemical sensors, and colorimetric sensors. While a number of sulfur sensors have been already available in the market, implementation of these sensors in FCs applications has been challenging due to various reasons as elaborated below.

Gas chromatography (GC)

GC coupled with FPD/PFPD (ASTM D6628-01 [44]) and SCD (ASTM D5504-01 [45], EPA 2000b) methods have been extensively used as ASTM standard methods to measure H_2S concentration in gaseous streams [46]. In these methods, H_2S is combusted in a hydrogen rich (H_2/Air) environment to produce electronically excited S_2^* (FPD/PFPD) and SO_2^* (SCD) species. These species emits characteristic light radiations when they come back from excited state to ground state. Subsequently, the radiations are detected by a photomultiplier tube (PMT). The PMT signal is usually linear to H_2S concentration.

These methods are accurate and sensitive to ppm level. However, ppb level sensing tends to show extreme nonlinear response behavior and requires difficult and frequent calibrations. For instance, they require large and laborious prepared samples to detect less than 100 ppb H_2S levels. The large sample size typically creates matrix overload causing a decreased signal to noise ratio which in turn deteriorating their quantification limits and selectivity. In addition, these methods require appropriate levels of oxygen and highly efficient combustion chamber operated at high temperature (i.e. 250 ^oC for FPD/PFPD and 850 ^oC for SCD leading to higher power consumption) for yielding correct excited characteristic species to avoid interference from other gas compositions. Moreover, they are expensive, and occupy large foot print due to complex systems. As a result of all these drawbacks in ppb level sensing, GC usage is limited in FCs applications.

Metal oxide semiconductors (MOS)

Metal oxide semiconductor (MOS) sensors are based on the change of conductivity of the sensing material, such as SnO_2, ZnO, In_2O_3, and WO_3 [47-54], with the interaction of H_2S. The shift of oxygen equilibrium reaction due to presence of reducing gas (H_2S) is the basis of their sensing mechanism. This equilibrium reaction can be categorized in two major steps. In step one, oxygen adsorbs to the n-type semiconductor MOS in the form of O^- or O_2^- ions depending on the operating temperature. These adsorbed oxygen ion creates a charge depletion region on the MOS surface due to the extraction of MOS conduction electrons. Hence, this adsorption process results in a decrease of MOS conductivity. In step two, the reducer gas (R) reacts with the adsorbed oxygen ions and release the electrons back to the MOS, resulting in an increase in the conductivity. Commonly, the change in MOS conductivity is proportional to the amount of reducer gas present in the atmosphere. The equilibrium gas response reactions can be given as [55]:

$$O_2(\text{gas}) + 2e^- \rightarrow 2O^-(\text{adsorbed}) \qquad \textbf{(Step 1)}$$

$$R + O_2^- \ (\text{adsorbed}) \rightarrow RO + e^- \qquad \textbf{(Step 2)}$$

The major disadvantage of these sensors is the shift of oxygen equilibrium reaction due to the reducer gas, which is not specific. This situation has negative effect for the detection of sulfur impurities in hydrogen fuels because a large amount of hydrogen gas acts as a reducer gas rather than the low levels of H_2S. As a result, the high concentration of hydrogen totally masks the signal from the sulfur. This selectivity issue confines their usage in hydrogen based FCs. Other shortcomings of this technique include high operating temperatures which are required to adsorb oxygen to the MOS, leading to high power consumption. Most of these sensors are restricted to ppm levels of detection. Besides, these MOS sensors show short linear dynamic range, and also the oxygen levels significantly alter the sensitivity of the sensor.

Electrochemical sensors (EC)

EC sensors are three electrode cells in which a sensing electrode and a counter electrode are separated by a thin layer of liquid electrolyte. H_2S gas analyte first passes through a diffusion membrane followed by an oxidation reaction at the anode (sensing electrode). This oxidation reaction changes the cell current and the cell current is proportional to the gas concentration [56-59]. The rate limiting step that determines the amount of output signal in this method is the rate of H_2S diffusion through the membrane to the sensing electrode. For instance, a porous hydrophobic membrane is generally employed to enhance the sensitivity of the electrochemical cell at low concentrations of gas analyte. To the downfall, this porous membrane allows the liquid electrolyte to escape from the cell leading to a short operating life. Therefore, these sensors need frequent recalibrations due to their high dependence on the climatic conditions which in turn limit their reliability. Additionally, majority of them are restricted to ppm level sensing. A major challenge of this type of EC sensor is the similar oxidation potential shown by the H_2S and H_2 reactions, making them unsuitable for sulfur monitoring in hydrogen operated FCs.

Colorimetric sensors

Colorimetric sensors are based on color change of the sensing material upon H_2S exposure. Paper tape method is one such method where moist H_2S gaseous sample is passed over lead-acetate impregnated paper at a constant flow rate. The paper tape forms a brown stain due to the reaction between H_2S and lead acetate. Subsequently, the change of color is detected by a spectrophotometer, and this rate of stain is proportional to the H_2S concentrations in the sample. According to ASTM D4048, this method can effectively detect low ppm levels of H_2S [60]. To date, these sensors have remained as widely used commercial instruments to measure ppm levels of H_2S. In this method, particular attention has to be given, such as passing the H_2S gas through the tape rather than passing by side of the tape for attaining accurate signal. Also, they need to be protected from light to avoid photo-bleaching.

An alternative colorimetric sensor for the detection of H_2S is based on the color change of chemoresponsive dyes upon sulfur exposure [61]. In this detection method, Sen and his co-workers demonstrated a colorimetric sensor array consisting of chemoresponsive dyes for monitoring humidified H_2S in N_2 gas flow. These dyes undergo a color change when H_2S gas was exposed for 30 minutes, and the magnitude of the color change depends on the $H_2S:N_2$ concentrations (50 ppb, 100 ppb, 250 ppb, and 500 ppb). The major disadvantage of this sensor is its long response time (e.g., 30 minutes) and possible interference from the other sulfur compounds (SO_X). Also, the underlying mechanism of this sensor was not explained clearly.

For the above mentioned reasons, now more than ever there is a need for advanced sensors to monitor H_2S impurities in trace levels especially in hydrogen gas.

CHAPTER III

METHODOLOGY

3.1 Fabrication of Si reducer film using plasma-enhanced chemical vapor deposition

Initially, 1737 Corning glass slide (3″ × 3″) was ultrasonicated in de-ionized (DI) water (18.2 MΩ) for 5 minutes followed by scrubbing with a soft nylon brush to remove any macroscopic impurities. Then, the glass slide was immersed in 35% isopropyl alcohol (IPA) in DI water solution and ultrasonicated for 10 minutes for organic cleaning. Next, the slide was cleaned in DI water for 10 minutes followed by blow drying with Ar. Finally, the cleaned glass slide was annealed on a hot plate (VWR 500 Series) at 150 ^{o}C for 10 minutes to remove any adsorbed water before Si deposition.

Si deposition was performed by using Plasma-Therm 790+ model plasma-enhanced chemical vapor deposition (PECVD) system. The Si film serves as a reducer during the electroless reduction of the silver nanoparticles (Ag NPs) in this work. Specifications of the deposition chamber are as follows. Diameter of the deposition chamber is 667 mm and the frequency of RF amplifier is 13.56 MHz with an output power of 100W. The Si deposition was performed in the following way. The cleaned glass slide was first loaded into the deposition chamber and then plasma was created through capacitive induction of the RF amplifier. A mixture of silane (SiH_4) and helium (He) in a ratio of 1:99 was used as the precursor gas and supplied to the system with a flow rate of 1200 sccm. Finally, Si deposition was carried out for 5 min and 50 s until an approximate value of 50 nm of thickness was reached onto the glass substrate, which was kept at 250 ^oC. The base pressure was maintained at $<10^{-6}$ Torr and the process pressure was kept at 1 Torr during the deposition.

Figure 3.1: Plasma-Therm 790+ PECVD system that was employed for Si deposition. The system is located at Henry Research Center, Oklahoma State University, Tulsa, OK. (Source: Plasma-Therm 790+ PECVD system instruction catalogue)

3.2 Nanoparticle synthesis by electroless reduction technique

Ag NPs were synthesized as illustrated in Fig. 3.2. The Si on glass substrates were first diced to 1 cm × 0.5 cm chips. Then, they were immersed in 0.002 M $AgNO_3$ + 0.1% HF in water for 20 s, and the reaction was then stopped immediately by immersing the Si films in DI water. Finally, the sample was blown dried by Ar. Here, Ag NPs are formed by the reduction of Ag^+ ions in the $AgNO_3$ by the silicon film. During the synthesis, Si electrons are used for reducing Ag^+ by concomitantly forming a silicon oxide layer on the

Si surface. The primary role of HF in the solution is to constantly etch away this oxide layer that inhibits silver nucleation during the redox reaction [15].

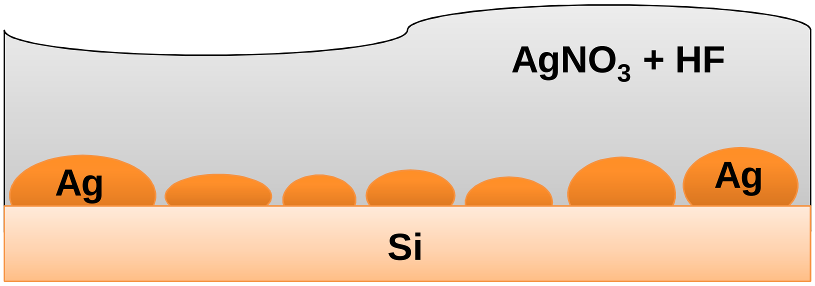

Figure 3.2: Schematic showing the electroless reduction of Ag NPs on the Si film using 0.002 M $AgNO_3$ + 0.1% HF solution.

3.3 Extinction measurements

Figure 3.3 illustrates the optical cell enclosing the sample that is held against the wall of the optical cell with a stainless steel (SS) spring. A butyl rubber septum was used to seal the screw cap of the vial. Initially, the vial is purged with argon (Ar) for 8 minutes. Then it was exposed to a pre-concentrated H_2S in H_2 gas flow.

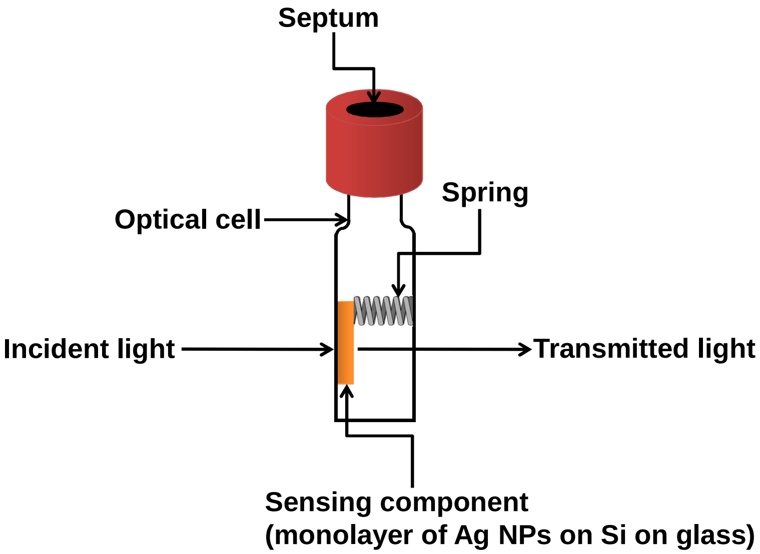

Figure 3.3: Diagram illustrating the optical cell consisting of sample (Ag NPs on Si on glass) held by a spring.

The optical extinction of the Ag NPs was acquired using StellerNet EPP 2000Cs UV-visible spectrometer, equipped with a CCD detector. The data were recorded with an integration time of 100 ms and 5 scans to average in the wavelength range of 190-900 nm. A Si on glass substrate was used as a reference to measure the extinction of the Ag NPs (Extinction $_{(Ag+Si+glass)}$ − Extinction $_{(Si+glass)}$). Finally, the extinction spectrum was fitted with Guassian function using Origin 8.1 software to extract extinction parameters, such as, peak position, peak intensity, and full width at half maximum (FWHM). The Origin software Guassian formula and sample curve (Fig. 3.4) are as follows:

$$y = y_o + \frac{A}{w \cdot \sqrt{\pi/2}} \cdot e^{-2\cdot(x-x_c)^2/w^2}$$

where, x_c = peak position, $w_1 = w/\sqrt{\ln(4)}$ = full width at half maximum (FWHM), y = peak intensity, and y_o = baseline

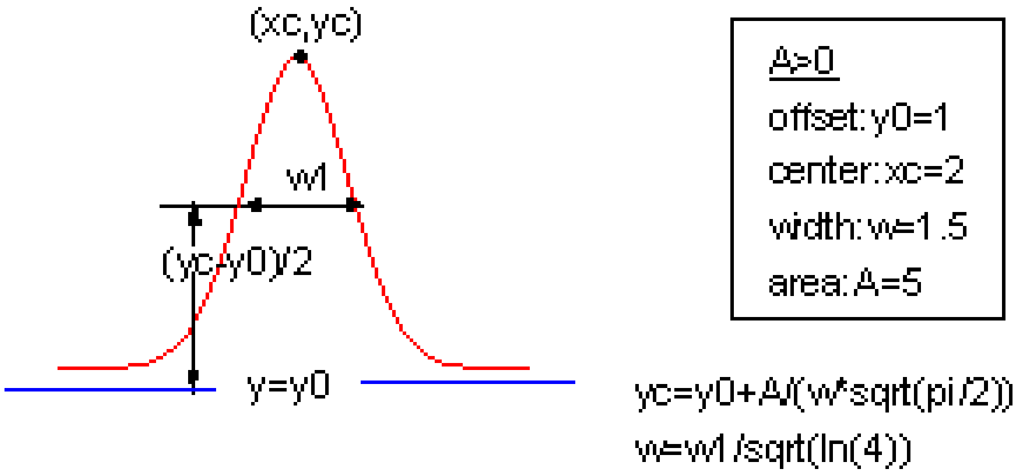

Figure 3.4: Sample curve of the Origin Guassian function that is used for the extraction of the extinction parameters. In this curve, w1 parameter represents full width at half maximum (FWHM). (Source: Origin 8.1 Tutorials)

3.4 H_2S exposure and sensing setup

1 ppm hydrogen sulfide (H_2S) in hydrogen (H_2) was purchased from Air Liquide specialty gases (Scott gas) company. This gas was then diluted to the desired concentration of 225 ppb, 120 ppb, and 65 ppb by mixing with ultrapure H_2 purchased from Stillwater Steel & Welding Supply (Stillwater, Oklahoma) as illustrated in Fig. 3.5. Two variable area flow meters purchased from Swagelok (G-series) were used to regulate the flow of H_2 and H_2S for mixing. A T-junction was provided to ensure proper mixing of both the gases and also a valve for effective control to mix gases. Finally, the pre-concentrated H_2S in H_2 gas flow was introduced into the vial through an inlet channel. Simultaneously, the exposed gas was directed to fume hood vent via the outlet channel.

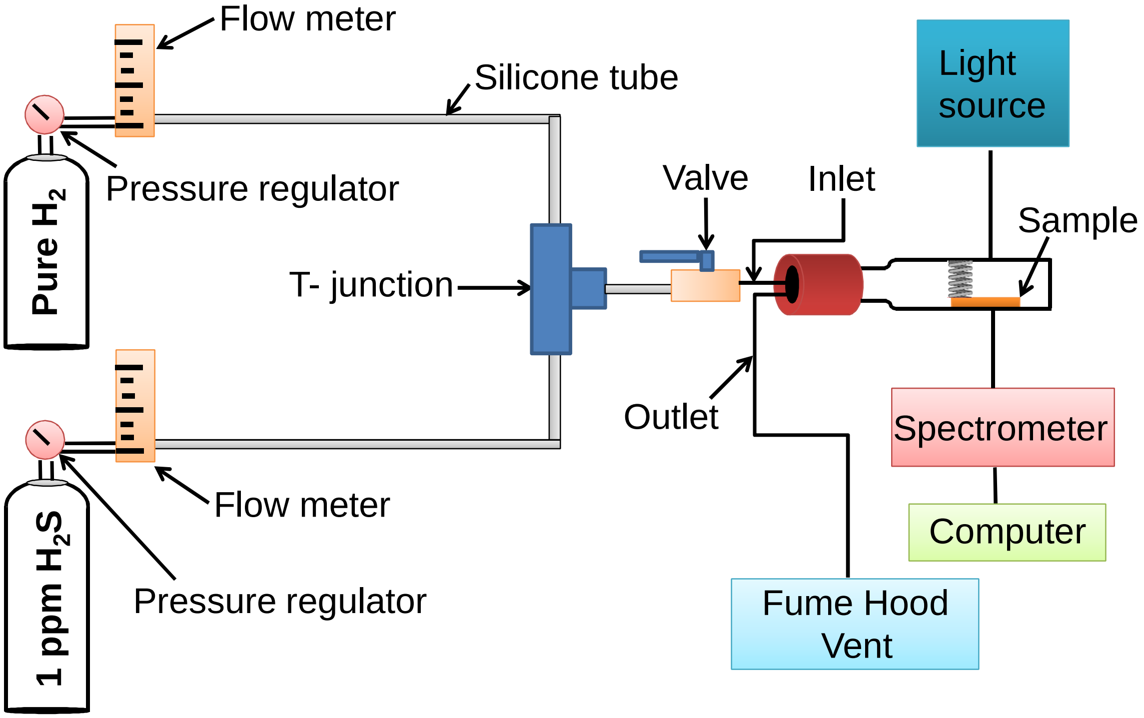

Figure 3.5: Sketch of the experimental setup for 1 ppm H_2S mixing with pure H_2 gas using regulators and flow meters.

3.5 Characterization of silver nanoparticles

A Veeco Multimode V scanning probe microscope (SPM) was employed to characterize the morphology of the Ag NPs synthesized by electroless reduction technique. The SPM was operated in Tapping Mode to scan topography of the Ag NPs. A double sided sticky tape was used to fix the sample firmly on a metal stub. 'MikroMasch' manufactured silicon cantilever NSC14/50 was utilized to obtain height measurements of the Ag NPs on Si film. The scans were performed in a 1 μm × 1 μm region with a scan rate of 1 Hz. The scans used 256 sampling points per line.

3.6 Raman scattering spectroscopy measurements

Renishaw RM 100 micro Raman spectroscopy coupled with a CCD camera and Leica DMLA microscope was used to identify the surface chemical species. Raman scattering measurements were carried out at an Ar^+ laser wavelength of 514 nm. A 20X objective lens with numerical aperture of 0.4 was used to focus laser on the substrate. Laser power of 3.5 mW and an accumulation of 200 s were used to record Raman scattering spectrum.

CHAPTER IV

RESULTS AND DISCUSSION

4.1 AFM characterization of silver nanoparticles

Figure 4.1 shows an AFM tapping mode scanning image of Ag NPs on Si film. The Ag NPs were synthesized by using the electroless reduction technique, which was elaborated in Section 3.2. The inset histogram in Fig. 4.1 provides the Ag NP size distribution. The average size of the NP is determined to be 36 nm. The average height of the NP is found about half of the diameter (17.5 nm), indicative of a hemispherical shape.

Compared to the previous work conducted by Kalkan and co-workers [16], the Ag NPs in the present work showed a more inhomogeneous distribution (Fig. 4.1). This higher inhomogeneity is primarily attributed to lower Fermi energy difference ($\Delta E_F \approx 0.3$ eV) between the Ag NPs ($E_F = 4.3$ eV) and the lower band gap a-Si film ($E_F \approx 4.6$ eV, measured from the vacuum level) [62]. In contrast, earlier demonstrations by Kalkan group employed $\Delta E_F = 0.85$ eV.

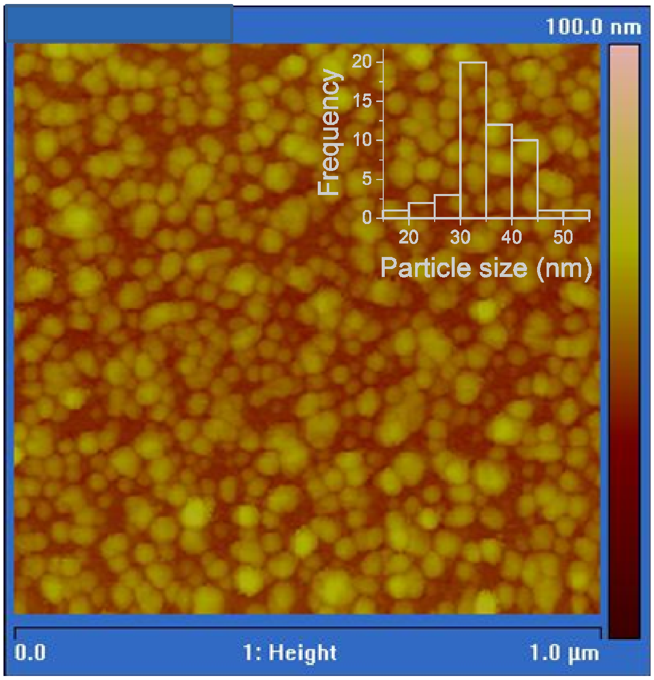

Figure 4.1: AFM image of the Ag NPs reduced on Si substrate. The inset histogram provides the NP size distribution.

4.2 Extinction of silver nanoparticles

Ag NPs on Si substrate were characterized by the extinction spectroscopy as described in Section 3.3. The extinction spectrum of the as-prepared Ag NPs displayed two peaks (Fig. 4.2). As observed in the AFM image of Fig. 4.1, closely distributed NPs lead to the hybrid plasmon resonance (see Section 2.2) as indicated by higher-wavelength peak centered at 485 nm. On the other hand, the lower-wavelength peak is attributed to a combination of quadrupole and regular dipolar bands that are convoluted together. Typically, NPs larger than 30 nm in size exhibit quadrupole band, and well-isolated NPs exhibit a distinct regular dipolar band. It can be seen that these peaks are subdued as indicated by their extinction strengths (i.e., peak heights) compared to the hybrid-resonance peak.

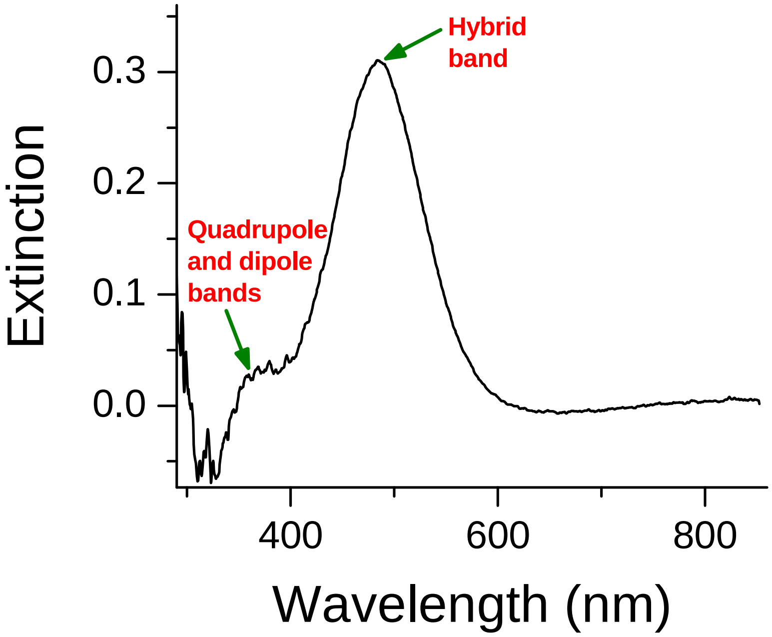

Figure 4.2: Extinction spectrum of the Ag NPs reduced on Si substrate.

To further understand the nature of the plasmon peaks, methanol based experiments were performed. The extinction spectrum of the supported Ag NPs immersed in methanol (99.99% ACS grade) was recorded right after the immersion and after 52 hours of immersion (Fig. 4.3). Methanol molecules adsorb onto the Ag NPs with their OH group. They act as surfactant and lift off the weakly attached NPs from the Si surface over time [63]. Extinction measurements displayed an increase in extinction and a red shift in the lower-wavelength extinction peak. Simultaneously, a significant reduction in the intensity of the peak centered at 485 nm was observed when the Ag NPs were soaked in methanol for 52 hours. Upon methanol adsorption, some of the interacting NPs lift off from the surface. This event increases the number of non-interacting particles that contribute to the regular dipolar-plasmon band. An effective increase in the regular dipolar-plasmon band intensity is seen in the spectra shown in Fig. 4.3. Disappearance of the hybrid band shown by the downward arrow in Fig. 4.3 substantiates a significant increase in the interparticle distance. These results corroborate the previous assignments on the extinction peaks.

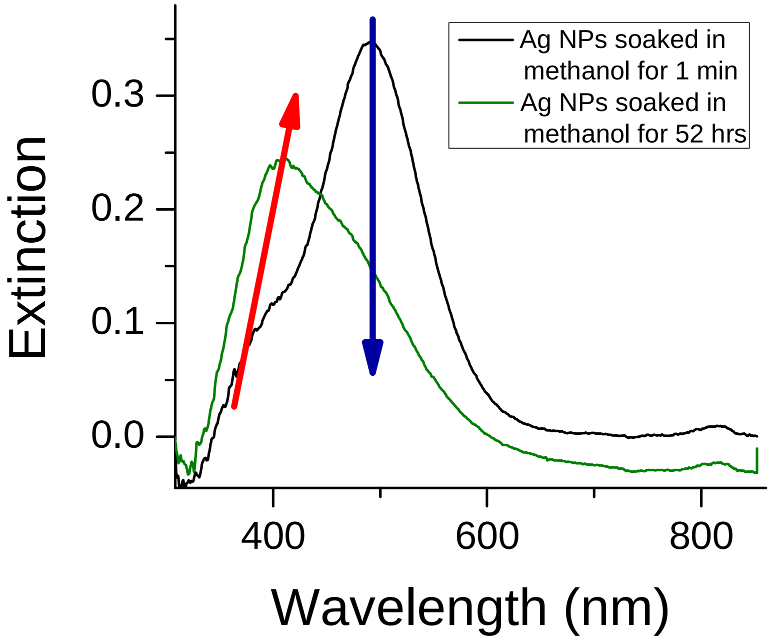

Figure 4.3: Extinction spectra of the supported Ag NPs before and after immersion in methanol. The blue arrow indicates the fading of the hybrid plasmon extinction. The red arrow shows increase of the regular dipolar plasmon extinction.

4.3 Extraction of extinction parameters

The extinction spectrum of the Ag NPs was fitted to Gaussian function using Origin 8.1 software. Parameters associated with the line shape, such as full width at half-maximum (FWHM), extinction, and peak position were extracted as described in Section 3.3. Figure 4.4 shows a typical Gaussian fit to the extinction spectrum. In reality, the extinction spectrum for a single NP is expected to be Lorentzian with a much lower FWHM. Therefore, the observed Gaussian nature of the peak is attributed to the interparticle distance distribution as well as size and shape distribution of the particles.

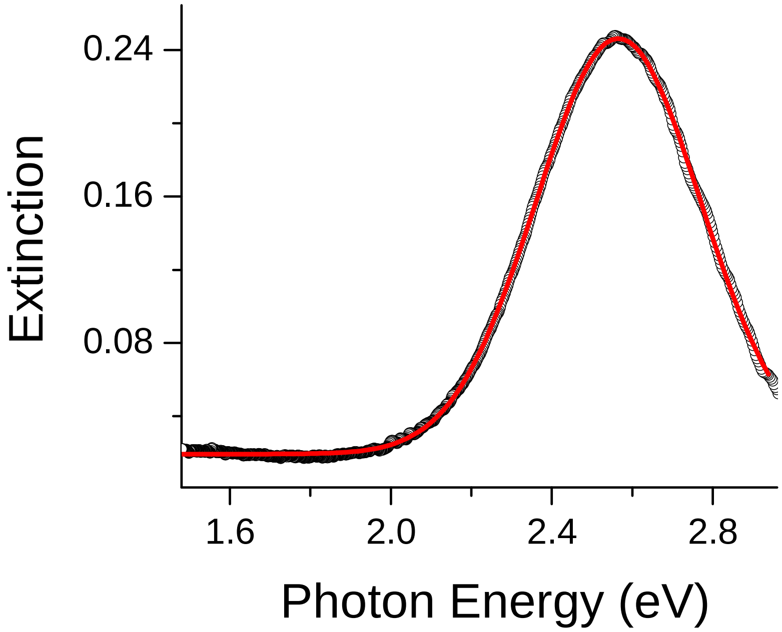

Figure 4.4: Ag NPs extinction spectrum fitted to Gaussian function (red). Extinction parameters such as FWHM, extinction, and peak position are extracted from this fit function.

The Gaussian fit in Fig. 4.4 is simply the envelope function for the multiple Lorentzian peaks that are convoluted together. It is important to note that the FWHM associated with the Gaussian fit does not represent the damping factor (Γ) directly since the Gaussian FWHM includes both homogenous broadening (damping) as well as heterogeneous broadening (distribution). However, a relation may be established between the damping factor (Γ) and FWHM.

4.4 Relation of full width at half maximum (FWHM) with damping factor (Γ)

To understand the relation between the FWHM of the extinction band and the damping factor (Γ), the extinction band is fitted with a Voigt function, which is the convoluted form of Lorentzians by a Gaussian envelope. By definition, the Voigt function is given by [64]:

$$V(x) = \int_{-\infty}^{+\infty} G(x_o) \cdot L(x - x_o) \cdot dx_o \qquad (4.1)$$

where, x is frequency from the center line.

The Gaussian function with a standard deviation (σ) is:

$$G(x) = \frac{e^{(-x^2/2\sigma^2)}}{\sigma\sqrt{2\cdot\pi}} \qquad (4.2)$$

FWHM of the Gaussian peak can be obtained by,

$$\Gamma_G = 2\sigma \cdot \sqrt{2 \cdot \ln(2)} \qquad (4.3)$$

The Lorentzian function is given by:

$$L(x) = \frac{\Gamma/2}{\pi \cdot (x^2 + \Gamma^2/4)} \qquad (4.4)$$

where, Γ is the FWHM of the Lorentzian peak, that is, damping factor (Γ) for a single NP. After proper substitutions, the FWHM of the Voigt profile that is largely of Gaussian nature can be approximated as [65]:

$$\Gamma_V \approx 0.53 \cdot \Gamma + \sqrt{0.21 \cdot \Gamma^2 + {\Gamma_G}^2} \qquad (4.5)$$

Next, to determine the relation between the change in the Lorentzian FWHM (Γ) and the Voigt FWHM (Γ_V), a linear differential approximation is performed as follows:

$$\Delta\Gamma_V = \frac{d\Gamma_V}{d\Gamma} \cdot \Delta\Gamma = \left\{0.53 + 0.5 \cdot (0.21 \cdot \Gamma^2 + {\Gamma_G}^2)^{-1/2} \cdot (0.42 \cdot \Gamma)\right\} \cdot \Delta\Gamma \qquad (4.6)$$

Let us consider the term, $(0.21 \cdot \Gamma^2 + {\Gamma_G}^2)^{-1/2}$, from Equation 4.6 which can be rewritten as:

$$\frac{1}{\Gamma_G \cdot \sqrt{0.21 \cdot (\frac{\Gamma}{\Gamma_G})^2 + 1}} \qquad (4.7)$$

Since the Voigt fit is largely of Gaussian (i.e., $\Gamma << \Gamma_G$), it implies:

$$(\Gamma / \Gamma_G)^2 << 1 \qquad (4.8)$$

Therefore, using the abovementioned relation, Equation 4.7 can be approximated as:

$$\frac{1}{\Gamma_G \cdot \sqrt{0.21 \cdot (\frac{\Gamma}{\Gamma_G})^2 + 1}} \approx \frac{1}{\Gamma_G} \qquad (4.9)$$

Then, by substituting the value of Equation 4.9, the term from Equation 4.6 can be approximated as:

$$0.5 \cdot (0.21 \cdot \Gamma^2 + \Gamma_G{}^2)^{-1/2} \cdot (0.42 \cdot \Gamma) \approx 0.21 \cdot (\Gamma / \Gamma_G) \qquad (4.10)$$

As stated earlier, the Voigt fit is largely of Guassian (i.e., $\Gamma << \Gamma_G$). Therefore, Equation 4.10 can be further approximated as:

$$0.5 \cdot (0.21 \cdot \Gamma^2 + \Gamma_G{}^2)^{-1/2} \cdot (0.42 \cdot \Gamma) \approx 0.21 \cdot (\Gamma / \Gamma_G) \approx 0 \qquad (4.11)$$

Now, by plugging the value of Equation 4.11, Equation 4.6 can finally be approximated as:

$$\Delta\Gamma_V \approx \Delta\Gamma_G \approx 0.53 \cdot \Delta\Gamma \qquad (4.12)$$

Thus, Equation 4.12 establishes the relation between the change in Voigt and/or Gaussian FWHM and the damping factor (Γ) change. In this analysis, Γ is considered to be constant, and the Gaussian broadening is attributed to the distribution of maxima of Lorentzians. Figure 4.5 displays Voigt and Gaussian fits to a representative Ag NPs extinction spectrum. Both fits show a good fit with adjusted R-square of 99.96 percent.

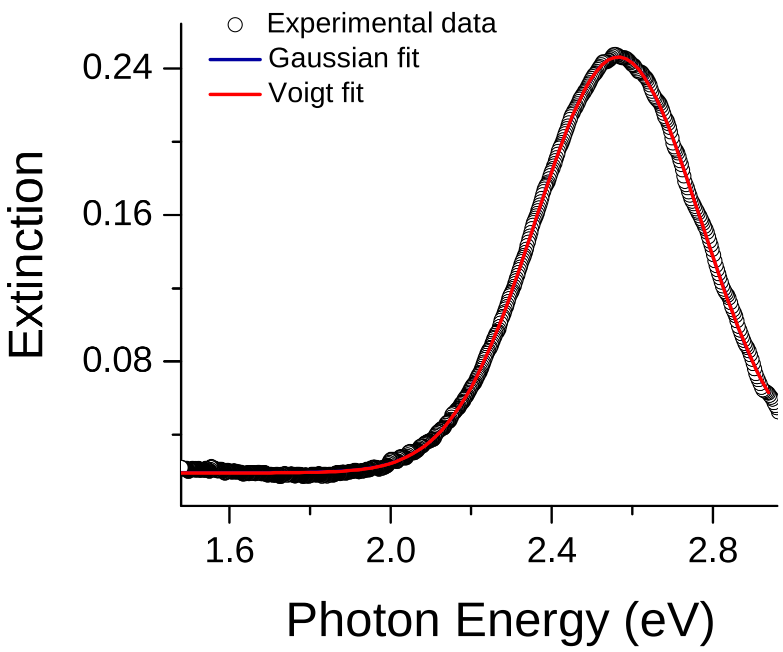

Figure 4.5: Ag NPs extinction spectrum fitted to Gaussian and Voigt functions.

4.5 Sensor response to H_2S impurity in H_2

Figure 4.6 shows extinction spectra of the Ag NPs that were exposed to H_2 gas flow of 320 ppb H_2S impurity as elaborated in Section 3.4. The extinction spectra were captured for a total period of 220 s with a time interval of 3 s. The plot shown in Fig. 4.7a indicates the increase in FWHM with time. This increase in FWHM in turn decreases the peak intensity as shown in Fig. 4.7b. H_2S molecules adsorbed on the Ag NPs increase the plasmon-damping by chemical interface damping (CID) and surface scattering by inducing electric potential perturbations on the NP surface as explained in Section 2.4. Also, it was observed that the hybrid plasmon resonance peak initially shifted to higher energies and later shifted gradually towards lower energies. The peak position change with time is depicted in Fig. 4.7c. This peculiar observation can be explained as follows.

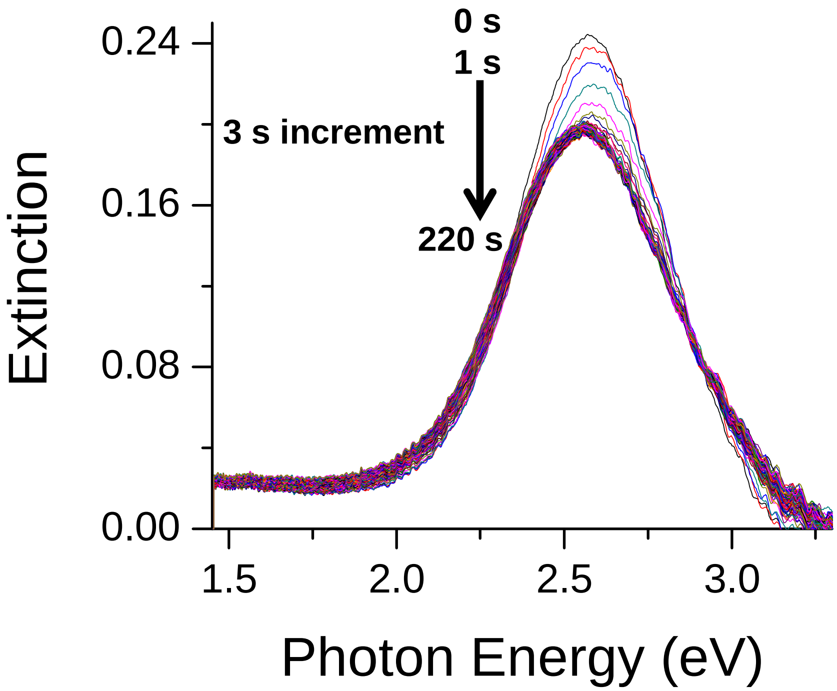

Figure 4.6: Time series extinction spectra of the Ag NPs being exposed to 320 ppb H_2S in 380 sccm H_2 gas flow. The spectra are captured at 3 s intervals from 1 to 220 s. Here, 0 s represents the spectrum that was recorded before H_2S exposure.

The sulfur atom of the H_2S molecule most likely makes a dative bond with Ag NP by donating its extra lone pair of electrons to a dangling bond of d-orbital nature. This dative bond formation increases the electron density of the NP, resulting in an increase in bulk plasmon frequency as well as localized surface plasmon frequency, namely a blue shift in the plasmon peak position. On the other hand, the subsequent gradual shift of the plasmon hybrid mode peak position to lower energies (red) can be explained by relaxation of Ag−S dative bonds to covalent bonds, which this time leads to: i) decrease in the NP electron density; ii) increase in dielectric constant of the medium surrounding the NPs. Both changes account for the frequency decrease of the regular plasmon resonance or equivalently to a red shift in the hybrid plasmon resonance.

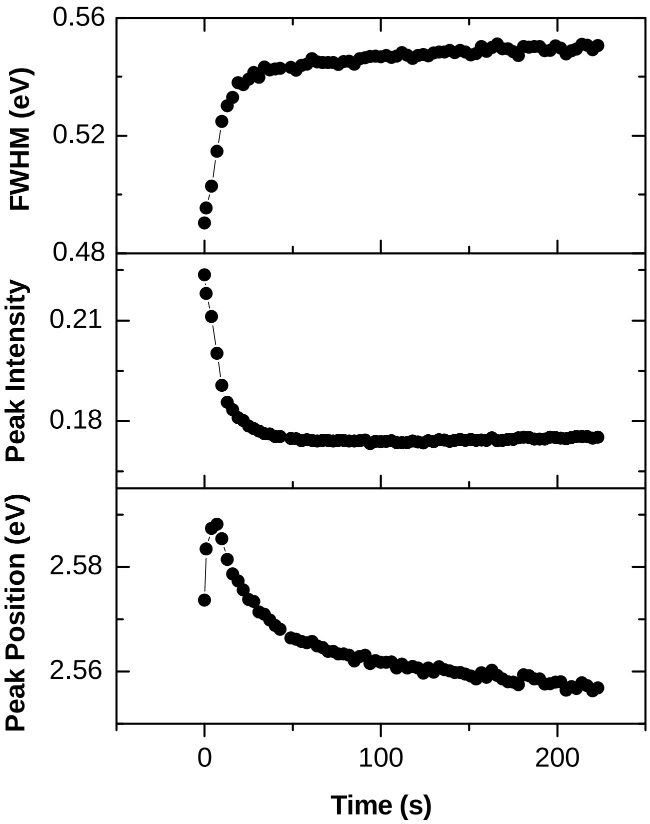

Figure 4.7: Time series change in FWHM (a), extinction (b), and peak energy (c) of the Ag NPs when exposed to 320 ppb H_2S in 380 sccm of H_2 gas flow.

4.6 Sensor response

The significance of the relation between the FWHM and Γ is that $\Delta\Gamma$ is proportional to the number of adsorbates (N_a) on the nanoparticle. Once, $\Delta\Gamma$ is shown to be proportional to ΔFWHM, then ΔFWHM is also proportional to the N_a. At chemical exposure time of t, the ΔFWHM is given by:

$$\Delta\text{FWHM}(t) = \text{FWHM}(t) - \text{FWHM}(t=0) \qquad (4.13)$$

The $\Delta FWHM$ of Equation 4.13 is observed to be a function which depends on gas concentration (C), gas flow rate (F), and exposure time (t). Therefore, the $\Delta FWHM$ can be expressed as:

$$\Delta FWHM = \Delta FWHM\,(C,F,t) \qquad (4.14)$$

In this thesis work, the gas flow rate (F) was fixed at 520 sccm. Based on this condition, Equation 4.14 can be written as:

$$\Delta FWHM\,(C,t) = FWHM\,(C,t) - FWHM\,(C,0) \qquad (4.15)$$

where, $FWHM\,(C,t)$ denotes the FWHM measured at a time t during H_2S exposure of concentration C, and $FWHM\,(C,0)$ represents the FWHM measured before H_2S exposure at time 0.

Figure 4.8 shows Ag NPs $\Delta FWHM$ when exposed to 225 ppb (a), 120 ppb (b), and 65 ppb (c) concentrations of H_2S in 520 sccm of H_2 gas flow. Three separate experiments were conducted for each concentration to verify the reproducibility. Figure 4.8 provides the $\Delta FWHM$ plots for different H_2S concentrations and their associated error bars. The insignificant error bars illustrate the sensor's good reproducibility.

A comparison of sensor response for 225 ppb, 120 ppb, and 65 ppb H_2S in H_2 is shown in Fig. 4.9. The pure hydrogen (~0 ppb H_2S) exposure showed almost no response. Obviously, the ΔFWHM is dependent on the H_2S concentrations as observed in Fig. 4.9.

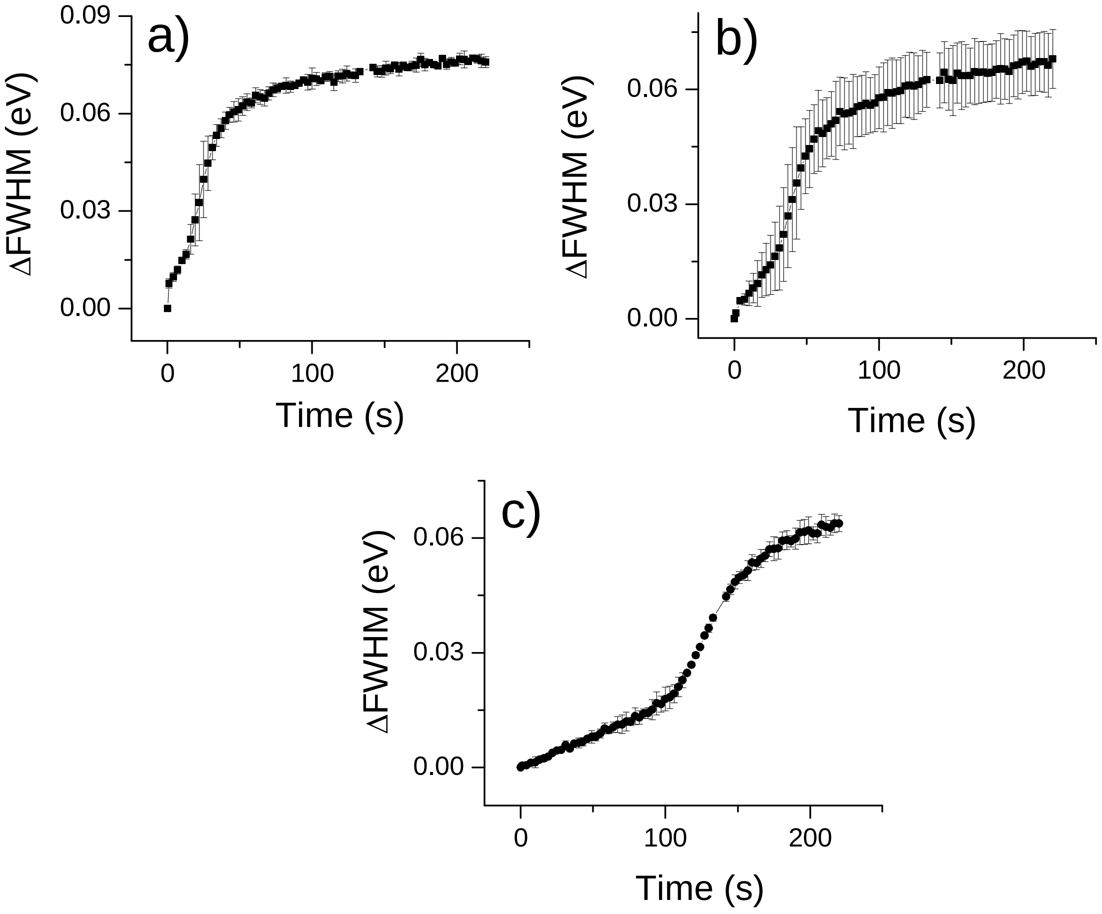

Figure 4.8: Change in hybrid plasmon-damping in Ag NPs upon exposure to 225 ppb H_2S (a), 120 ppb H_2S (b), and 65 ppb H_2S (c) in 520 sccm of H_2 gas flow. The associated error bars are shown.

4.7 Langmuir adsorption isotherms

The kinetics of ΔFWHM is found to follow the gas adsorption isotherm on a solid surface, expressed by the Langmuir equation:

$$\Delta FWHM = \frac{QCk_a}{Ck_a + k_d}(1 - e^{-(Ck_a + k_d)t}) \qquad (4.16)$$

where, Q is a proportionality constant, C is the H_2S concentration, and t is the time. Ck_a and k_d denote the rate of adsorption and desorption, respectively.

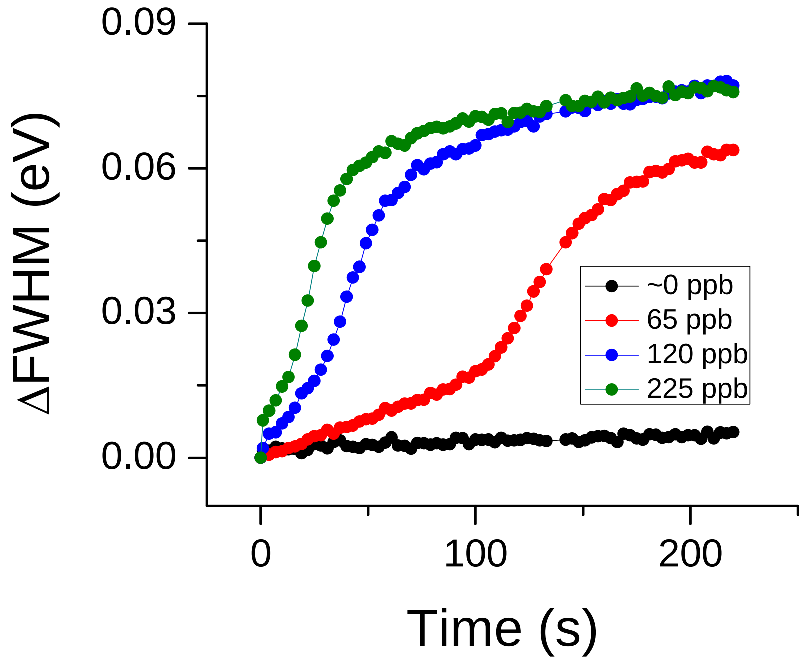

Figure 4.9: Sensor response to 225 ppb, 120 ppb, and 65 ppb H_2S in 520 sccm of H_2 gas flow compared to the pure hydrogen (~0 ppb H_2S) gas flow.

Typically, Langmuir adsorption isotherms consist of two major regimes: linear rise and saturation. By simple differentiation, the slope in the linear regime is calculated to be QCk_a, where Qk_a can be determined by sensor calibration measurements. Using Equation 4.16, concentration based on the saturation regime can be also be evaluated as $C = \Delta FWHM_{sat} \cdot k_d / (Q - \Delta FWHM_{sat}) \cdot k_a$. Here $\Delta FWHM_{sat}$ denotes the plateau value, and the rate coefficients, k_a and k_d, can be extracted from the sensor calibration measurements at saturation.

Interestingly, the measured $\Delta \mathrm{FWHM}$ displayed the superposition of multiple Langmuir isotherms as depicted in Fig. 4.10. Separate Langmuir isotherms beginning at different times clearly suggest that the adsorption is surface selective. We explain this behavior as follows: (110) facet exhibits the highest surface energy, followed by (100) and (111) [66]. Therefore, it is possible that sulfur adsorbates initially occupy the highest surface energy facet for highest energy lowering, followed by the lower surface energy facets. This hypothesis is based upon close to thermodynamic equilibrium conditions, which are enabled by sufficient surface diffusion. In Fig. 4.10, the overall fit to the $\Delta \mathrm{FWHM}$ kinetics includes the sum of adsorption isotherms associated with surface 1 and surface 2 of different energies. Remarkably, it is observed that the adsorption on surface 2 begins only after surface 1 almost reaches its saturation regime. The results in Fig. 4.9 indicate that the starting time of the surface 2 adsorption isotherm is shortened by the H_2S concentration. Hence, it is inferred that surface 2 starts to be occupied only after surface 1 is partially filled.

4.8 Determination of H_2S concentration using Langmuir's isotherm in the linear regime

In the present sensor calibration, the time rate of change of $\Delta \mathrm{FWHM}$ (i.e., slope) in the linear regime associated with surface 1 is considered for determining H_2S concentration. As mentioned earlier, the slope of the Langmuir isotherm at the linear regime, QCK_a, is proportional to the gas concentration. This scheme has enabled the present work to determine the H_2S concentration in as short as 10 s. Figure 4.11 shows this slope of $\Delta \mathrm{FWHM}$ for pre-concentrated H_2S:H_2 gas flows.

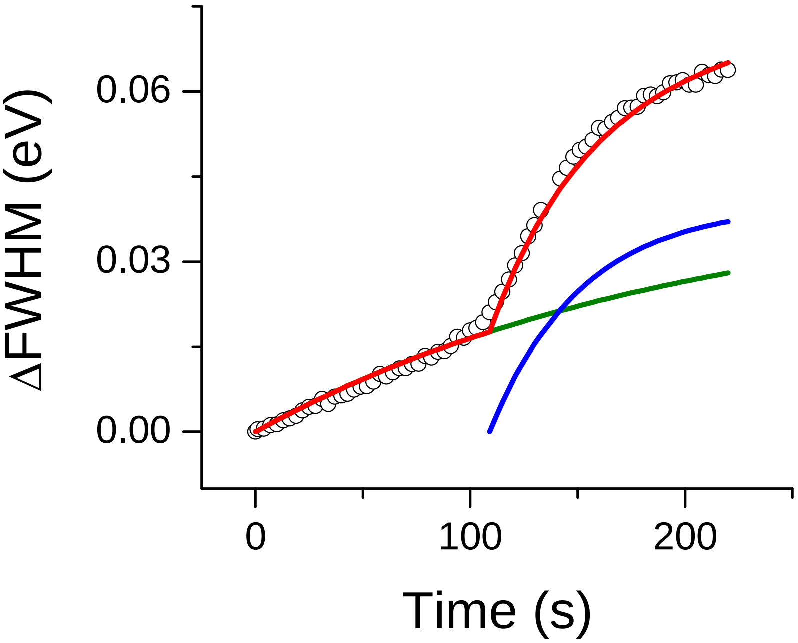

Figure 4.10: Fit of multiple Langmuir adsorption isotherms (solid red line) to the ΔFWHM kinetics (circles) for the 65 ppb H_2S in H_2 exposure case. Langmuir equation for surface 1 (green line) is $\Delta FWHM = 0.042 \times (1 - e^{-(0.005t)})$ and surface 2 (blue line) is $\Delta FWHM = 0.04 \times (1 - e^{-(0.0235 \times (t-109))})$. t is in seconds.

It is noticed that the linear fit for concentration versus slope in Fig. 4.11 yields a positive x-intercept at 50 ppb rather than passing through the origin of the plot. This intercept indicates that the H_2S concentrations below 50 ppb cannot be measured. At first, we attributed the offset of 50 ppb in Fig. 4.11 to a calibration error in mass flow controllers. Accordingly, we checked the flow rates in our operation range by monitoring the volume displacement in water. In result we observed only a minor deviation from the factory-calibration values that does not explain the offset in Fig. 4.11. Similarly, one can associate the offset with a lower concentration of H_2S in the H_2S:H_2 cylinder. However, this situation would only impact the slope of the line in Fig. 4.11 and not cause a parallel shift of the line. Accordingly, we explain the offset by what we call a “scavenging effect,” which lowers the H_2S gas concentration by 50 ppb no matter what the concentration is set to. This effect is possible if an impurity molecule sources from the H_2-dilution cylinder and rapidly reacts with H_2S. The flow rate of the dilution H_2 only changes by 20 percent, and hence the scavenging effect due to this impurity molecule will not vary significantly, accounting for the parallel shift. Another possibility is the production of H radicals on the Ag nanoparticles, which react with the H_2S above the Ag surface and scavenge it. The scavenging effect does not happen with the H_2S adsorbed to Ag because extended pure H_2 exposure does not regenerate the sensor.

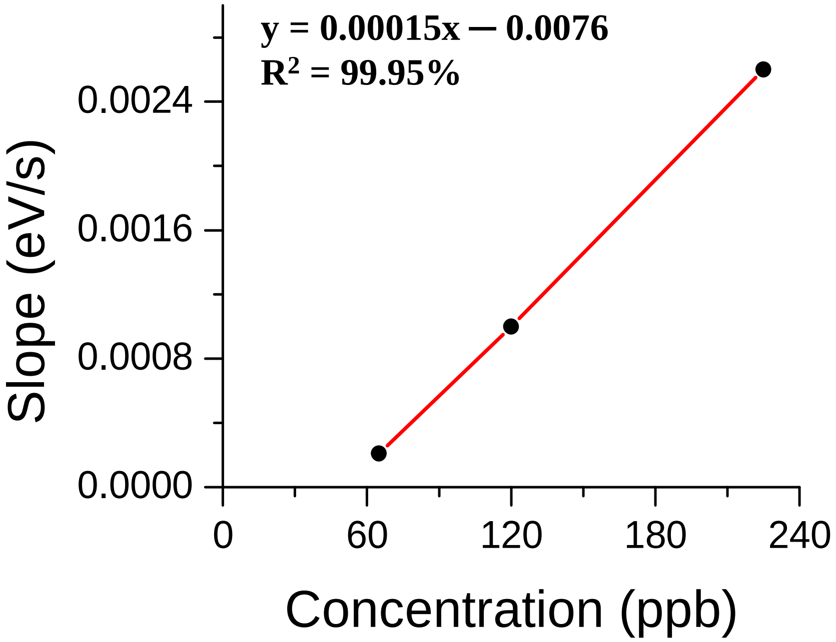

Figure 4.11: Calibration line showing the ΔFWHM surface 1 linear regime slope to the pre- concentrated H_2S:H_2-gas flows. The equation of the calibration line is shown.

4.9 Surface reaction study by surface−enhanced Raman spectroscopy

Chemical interaction of H_2S molecules with the Ag NPs surface was studied by Raman spectroscopy. Raman spectra were recorded as described in Section 3.6. Upon interaction with the Ag NPs, H_2S molecules chemisorb on the Ag NP surface in one of the following ways:

$$\mathrm{Ag} + \mathrm{H_2S} \rightarrow \mathrm{Ag\text{-}SH_{2,ads}} \qquad (4.17a)$$

$$\mathrm{Ag} + \mathrm{H_2S} \rightarrow \mathrm{Ag\text{-}SH_{ads}} + \mathrm{H} \qquad (4.17b)$$

$$2\mathrm{Ag} + \mathrm{H_2S} \rightarrow \mathrm{Ag_2S_{ads}} + \mathrm{H_2}\uparrow \qquad (4.17c)$$

According to the literature, the abovementioned nature of nondissociative or dissociative adsorption is still in debate [67, 68]. In general, Ag−S stretching mode shows a weak Raman peak in the range between 200−300 $\mathrm{cm^{-1}}$. However, a strong Raman peak associated with the Ag−S stretching mode is observed in the present thesis work. This amplification in the spectroscopic peak is ascribed to surface-enhanced Raman scattering (SERS), which arises due to the local electromagnetic-field enhancement developed near the NP by LSPR [69]. Figure 4.12 displays the SERS spectra of the Ag NPs that are exposed to Ar, 500 ppb H_2S in H_2, and pure H_2 gas flows at a flow rate of 520 sccm for 5 minutes. Clearly, the SERS spectrum reveals the reaction of H_2S with the present Ag NPs by showing a rather unique 235 $\mathrm{cm^{-1}}$ peak in contrast to the pure H_2 and Ar exposures. For this reason, the 235 $\mathrm{cm^{-1}}$ signature peak is assigned to Ag−S stretching mode, which is in accord with the previous studies [70, 71]. The broad band at 480 $\mathrm{cm^{-1}}$ in the SERS spectra denotes the background signal (i.e., amorphous Si).

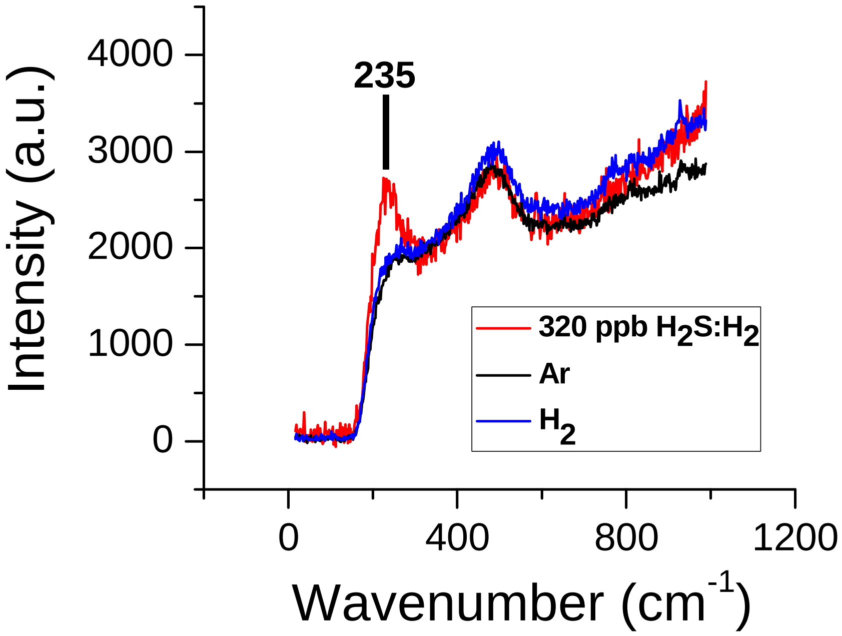

Figure 4.12: SERS spectra acquired from the sensor after the exposure of Ar, H_2S:H_2, and H_2. The peak at 235 cm^{-1} is ascribed to the Ag−S bond formation.

CHAPTER V

CONCLUSIONS AND FUTURE WORK

5.1 Conclusions

Important conclusions deduced from the present thesis work are listed below:

1. The present work demonstrates a novel chemical sensor for monitoring ppb level sulfur impurities in hydrogen fuels using the hybrid plasmon-resonance damping mechanism.
2. The change in plasmon-damping factor ($\Delta\Gamma$) of Ag NPs related to sulfur adsorption is observed to follow Langmuir adsorption isotherm consisting of linear and saturation regimes. This behavior suggests that the $\Delta\Gamma$ is also proportional to number of H_2S adsorbates.
3. Surprisingly, the kinetics of $\Delta\Gamma$ follows a multiple Langmuir adsorption isotherms. Superposition of two Langmuir isotherms starting at different times fits the $\Delta\Gamma$ kinetics. This behavior is chiefly attributed to the difference in surface energies of different crystal facets on the Ag NPs. It is anticipated that the H_2S adsorbs first to a higher energy surface, followed by an adsorption on the lower energy surface. Hence, it is anticipated that the surface diffusion is sufficiently high to ensure thermodynamic equilibrium.

4. The rate of change of $\Delta\Gamma$ (i.e., $d\Delta\Gamma/dt$ or slope) of the first Langmuir isotherm in linear regime plotted against the H_2S concentration has shown a linear relationship. This linearity is in agreement with the Langmuir's theory. Hence, the unknown H_2S gas concentration can be easily calculated from the simple linear calibration between the $d\Delta\Gamma/dt$ and concentration. Thus complex calibration procedures are avoided.
5. The lowest H_2S concentration detected by the sensor is 65 ppb. However, the sensing capability can go further down.
6. The present sensor response time is 10 s for H_2S:H_2-gas flow rate at 520 sccm through an optical cell (volume = 5.5 ml) having inlet and outlet channels. This small flow cell set-up allows forced convective-diffusion of sulfur adsorbates over the Ag NPs substrate. Therefore, a significant reduction in the response time is observed using a forced convective flow compared to diffusion- limited adsorption. Indeed, it is observed that the response time is highly dependent on the gas flow rate. For instance, the response time can be reduced to less than 10 s by simply increasing the gas flow rate above 520 sccm. As a result, the present sensor is highly attractive for rapid measurement of trace level sulfur impurities.
7. The insignificant error bars manifested by the $\Delta\Gamma$ kinetics for various H_2S concentrations prove the present sensor's good reproducibility. This characteristic demonstrates reproducible sensing of trace level H_2S impurities in H_2.
8. Although the present sensor showed a linear response to H_2S concentration, a negative intercept is observed in the linear calibration when the curve is extrapolated. This discrepancy is assigned to H_2 interference with the sensor's sensing ability, particularly for low H_2S concentrations (<50 ppb).

9. One of the important features of the present nanosensor is its integration capacity with a hand-held UV-visible spectrophotometer. For this reason, the miniature sensor design stands a significant commercialization potential.
10. Finally, the interaction of H_2S with the Ag NPs surface is characterized by the Raman scattering spectroscopy. The surface-enhanced Raman scattering (SERS) spectra confirmed the formation of Ag−S bond by clearly revealing a peak at 235 cm^{-1}, which is absent in the experiments conducted with pure H_2 and Ar.

5.2 Future work

The present nanosensor is a unique system to monitor molecular adsorption kinetics on metal surfaces based on the change in plasmon-damping factor ($\Delta\Gamma$). Specifically, this monitoring technique allows the tracing of Langmuir isotherms, enabling it a potential method in studying the surface reactions on noble metal NPs. For instance, self-assembly of alkanethiols ($(CH_2)_xX{-}SH$) onto Ag is an important surface process which can be monitored by the plasmon−damping sensing mechanism of the present work. Currently, this kind of work is already in progress under the supervision of Dr. Kaan Kalkan at Oklahoma State University, Stillwater.

The present Ag nanostructures, which exhibit the SERS effect can be utilized to study the nature of H_2S bonding (covalent or dative) with the Ag NP interface concomitantly with recording the extinction. For instance, if the H_2S molecule makes a dative bond by sharing its lone pair of electrons with Ag, then it should exhibit a S−H stretching mode in the SERS spectrum. On the contrary, the covalent bond formed through mutual sharing of electrons between S and Ag atoms should not exhibit the S−H stretching mode since it needs to be broken to allow the Ag−S chemical bond formation. Considering these insights, future work utilizing the Ag SERS substrates may elucidate the nature of H_2S bonding to the Ag NPs surface.

In the present thesis work, the way the sensor is employed in a disposable fashion. However, the sensor can be made reversible by desorbing the adsorbed sulfur molecules on the Ag NPs using an external energy source (heat or light energy). Nevertheless, the major challenge in the regeneration of the sensor lies in the selection of a valid energy exposure technique, which will desorb the sulfur bonded to silver without damaging the sensor.

REFERENCES

[1] U. S. Department of Energy. *Module 1: Hydrogen Properties* [Online]. Available: http://www1.eere.energy.gov/hydrogenandfuelcells/tech_validation/pdfs/fcm01r0.pdf

[2] U. S. Department of Energy. *Hydrogen and Our Energy Future* [Online]. Available: http://www1.eere.energy.gov/hydrogenandfuelcells/pdfs/hydrogenenergyfuture_web.pdf

[3] U. S. Department of Energy. *State of the States: Fuel Cells in America* [Online]. Available: http://www1.eere.energy.gov/hydrogenandfuelcells/pdfs/stateofthestates2011.pdf

[4] R. Mohtadi, W. K. Lee, S. Cowan, J. W. Van Zee, and M. Murthy, "Effects of hydrogen sulfide on the performance of a PEMFC," *Electrochemical and Solid-State Letters*, vol. 6, pp. A272-A274, 2003.

[5] V. A. Sethuraman and J. W. Weidner, "Analysis of sulfur poisoning on a PEM fuel cell electrode," *Electrochimica Acta*, vol. 55, pp. 5683-5694, 2010.

[6] U. Kreibig and M. Vollmer, *Optical Properties of Metal Clusters*: Springer, 1995.

[7] L. J. Sherry, R. Jin, C. A. Mirkin, G. C. Schatz, and R. P. Van Duyne, "Localized surface plasmon resonance spectroscopy of single silver triangular nanoprisms," *Nano Letters*, vol. 6, pp. 2060-2065, 2006.

[8] S. R. Beeram and F. P. Zamborini, "Selective attachment of antibodies to the edges of gold nanostructures for enhanced localized surface plasmon resonance biosensing," *Journal of American Chemical Society*, vol. 131, pp. 11689-11691, 2009.

[9] M. Fan, M. Thompson, M. L. Andrade, and A. G. Brolo, "Silver nanoparticles on a plastic platform for localized surface plasmon resonance biosensing," *Analytical Chemistry*, vol. 82, pp. 6350-6352, 2010.

[10] C. Wu and Q. H. Xu, "Stable and functionable mesoporous silica-coated gold nanorods as sensitive localized surface plasmon resonance (LSPR) nanosensors," *Langmuir,* vol. 25, pp. 9441-9446, 2009.

[11] A. J. Haes, W. P. Hall, L. Chang, W. L. Klein, and R. P. Van Duyne, "A localized surface plasmon resonance biosensor:□ First steps toward an assay for alzheimer's disease," *Nano Letters,* vol. 4, pp. 1029-1034, 2004.

[12] E. M. Larsson, J. Alegret, M. Käll, and D. S. Sutherland, "Sensing characteristics of NIR localized surface plasmon resonances in gold nanorings for application as ultrasensitive Biosensors," *Nano Letters,* vol. 7, pp. 1256-1263, 2007.

[13] P. Mulvaney, J. Pérez-Juste, M. Giersig, L. M. Liz-Marzán, and C. Pecharromán, "Drastic surface plasmon mode shifts in gold nanorods due to electron charging," *Plasmonics,* vol. 1, pp. 61-66, 2006.

[14] H. Hövel, S. Fritz, A. Hilger, U. Kreibig, and M. Vollmer, "Width of cluster plasmon resonances: Bulk dielectric functions and chemical interface damping," *Physical Review B,* vol. 48, pp. 18178-18188, 1993.

[15] A. K. Kalkan and S. J. Fonash, "Electroless synthesis of Ag nanoparticles on deposited nanostructured Si films," *The Journal of Physical Chemistry B,* vol. 109, pp. 20779-20785, 2005.

[16] K. Bhatt, S. Tan, S. Karumuri, and A. K. Kalkan, "Charge-selective Raman scattering and fluorescence quenching by “Nanometal on semiconductor” substrates," *Nano Letters,* vol. 10, pp. 3880-3887, 2010.

[17] S. Schultz, D. R. Smith, J. J. Mock, and D. A. Schultz, "Single-target molecule detection with nonbleaching multicolor optical immunolabels," *Proceedings of the National Academy of Sciences of the United States of America,* vol. 97, pp. 996-1001, 2000.

[18] M. Li, H. Schnablegger, and S. Mann, "Coupled synthesis and self-assembly of nanoparticles to give structures with controlled organization," *Nature,* vol. 402, pp. 393-395, 1999.

[19] M. E. Stewart, C. R. Anderton, L. B. Thompson, J. Maria, S. K. Gray, J. A. Rogers, and R. G. Nuzzo, "Nanostructured plasmonic sensors," *Chemical Reviews,* vol. 108, pp. 494-521, 2008.

[20] S. Link, Z. L. Wang, and M. A. El-Sayed, "Alloy formation of gold−silver nanoparticles and the dependence of the plasmon absorption on their composition," *The Journal of Physical Chemistry B,* vol. 103, pp. 3529-3533, 1999.

[21] L. M. Liz-Marzán, "Nanometals: Formation and color," *Materials Today,* vol. 7, pp. 26-31, 2004.

[22] P. Mulvaney, "Not all that's gold does glitter," *Materials Research Society Bulletin*, vol. 26, pp. 1-16, 2001.

[23] M. Faraday, "The bakerian lecture: Experimental relations of gold (and other metals) to light," *Philosophical Transactions of the Royal Society of London,* vol. 147, pp. 145-181, 1857.

[24] G. Mie, "Beiträge zur optik trüber medien speziell kolloidaler goldlösungen," *Annals of Physics,* vol. 25, pp. 377-445, 1908.

[25] K. L. Kelly, E. Coronado, L. L. Zhao, and G. C. Schatz, "The optical properties of metal nanoparticles: The influence of size, shape, and dielectric environment," *The Journal of Physical Chemistry B,* vol. 107, pp. 668-677, 2002.

[26] K.-S. Lee and M. A. El-Sayed, "Gold and silver nanoparticles in sensing and imaging: Sensitivity of plasmon response to size, shape, and metal composition," *The Journal of Physical Chemistry B,* vol. 110, pp. 19220-19225, 2006.

[27] C. Noguez, "Surface plasmons on metal nanoparticles: The influence of shape and physical environment," *The Journal of Physical Chemistry C,* vol. 111, pp. 3806-3819, 2007.

[28] P. Nordlander, C. Oubre, E. Prodan, K. Li, and M. I. Stockman, "Plasmon hybridization in nanoparticle dimers," *Nano Letters,* vol. 4, pp. 899-903, 2004.

[29] S. C. Yang, H. Kobori, C. L. He, M. H. Lin, H. Y. Chen, C. Li, M. Kanehara, T. Teranishi, and S. Gwo, "Plasmon hybridization in individual gold nanocrystal dimers: Direct observation of bright and dark modes," *Nano Letters,* vol. 10, pp. 632-637, 2010.

[30] P. K. Jain and M. A. El-Sayed, "Universal scaling of plasmon coupling in metal nanostructures: Extension from particle pairs to nanoshells," *Nano Letters,* vol. 7, pp. 2854-2858, 2007.

[31] C. A. Mirkin, R. L. Letsinger, R. C. Mucic, and J. J. Storhoff, "A DNA-based method for rationally assembling nanoparticles into macroscopic materials," *Nature,* vol. 382, pp. 607-609, 1996.

[32] R. Elghanian, J. J. Storhoff, R. C. Mucic, R. L. Letsinger, and C. A. Mirkin, "Selective colorimetric detection of polynucleotides based on the distance-dependent optical properties of gold nanoparticles," *Science,* vol. 277, pp. 1078-1081, 1997.

[33] S. Link and M. A. El-Sayed, "Size and temperature dependence of the plasmon absorption of colloidal gold nanoparticles," *Journal of Physical Chemistry B,* vol. 103, pp. 4212-4217, May 27 1999.

[34] F. Reynolds and G. Stilwell, "Mean free paths of electrons in evaporated metal films," *Physical Review,* vol. 88, pp. 418-419, 1952.

[35] U. Kreibig and C. V. Fragstein, "The limitation of electron mean free path in small silver particles," *Zeitschrift für Physik A Hadrons and Nuclei*, vol. 224, pp. 307-323, 1969.

[36] A. Wokaun, J. P. Gordon, and P. F. Liao, "Radiation damping in surface-enhanced Raman scattering," *Physical Review Letters,* vol. 48, pp. 957-960, 1982.

[37] A. Pinchuk and U. Kreibig, "Interface decay channel of particle surface plasmon resonance," *New Journal of Physics,* vol. 5, 2003.

[38] P. B. Johnson and R. W. Christy, "Optical constants of the noble metals," *Physical Review B,* vol. 6, pp. 4370-4379, 1972.

[39] M. Rycenga, C. M. Cobley, J. Zeng, W. Li, C. H. Moran, Q. Zhang, D. Qin, and Y. Xia, "Controlling the synthesis and assembly of silver nanostructures for plasmonic applications," *Chemical Reviews,* vol. 111, pp. 3669-3712, 2011.

[40] K. A. Willets and R. P. Van Duyne, "Localized surface plasmon resonance spectroscopy and sensing," *Annu Rev Phys Chem*, vol. 58, pp. 267-97, 2007.

[41] L. E. Kreno, J. T. Hupp, and R. P. Van Duyne, "Metal−organic framework thin film for enhanced localized surface plasmon resonance gas sensing," *Analytical Chemistry,* vol. 82, pp. 8042-8046, 2010.

[42] J. M. Bingham, J. N. Anker, L. E. Kreno, and R. P. Van Duyne, "Gas sensing with high-resolution localized surface plasmon resonance spectroscopy," *Journal of American Chemical Society,* vol. 132, pp. 17358-17359, 2010.

[43] K. M. Mayer and J. H. Hafner, "Localized surface plasmon resonance sensors," *Chemical Review,* vol. 111, pp. 3828-57, 2011.

[44] *Standard Test Method for Determination of Sulfur Compounds in Natural Gas and Gaseous Fuels by Gas Chromotography and Flame Photometric Detection,* ASTM International D6228, 2010.

[45] *Standard Test Method for Determination of Sulfur Compounds in Natural Gas and Gaseous Fuels by Gas Chromotography and Chemiluminescence,* ASTM International D5504, 2008.

[46] *Standard Practice for Gas Chromotograph Based On-line/At-line Analysis for Sulfur Content of Gaseous Fuels,* ASTM International D7165, 2010.

[47] S. S. Badadhe and I. S. Mulla, "H_2S gas sensitive indium-doped ZnO thin films: Preparation and characterization," *Sensors and Actuators B: Chemical*, vol. 143, pp. 164-170, 2009.

[48] D. D.J, "Surface chemistry of gas sensors: H_2S on WO_3 films," *Sensors and Actuators B: Chemical,* vol. 5, pp. 155-159, 1991.

[49] B. Frühberger, M. Grunze, and D. J. Dwyer, "Surface chemistry of H_2S-sensitive tungsten oxide films," *Sensors and Actuators B: Chemical,* vol. 31, pp. 167-174, 1996.

[50] C. S. Rout, M. Hegde, and C. N. R. Rao, "H_2S sensors based on tungsten oxide nanostructures," *Sensors and Actuators B: Chemical,* vol. 128, pp. 488-493, 2008.

[51] C. Wang, X. Chu, and M. Wu, "Detection of H_2S down to ppb levels at room temperature using sensors based on ZnO nanorods," *Sensors and Actuators B: Chemical,* vol. 113, pp. 320-323, 2006.

[52] J. T. L. Royster, D. Chatterjee, G. R. Paz-Pujalt, and C. A. Marrese, "Fabrication and evaluation of thin-film solid-state sensors for hydrogen sulfide detection," *Sensors and Actuators B: Chemical,* vol. 53, pp. 155-162, 1998.

[53] C. M. Ghimbeu, M. Lumbreras, J. Schoonman, and M. Siadat, "Electrosprayed metal oxide semiconductor films for sensitive and selective detection of hydrogen sulfide," *Sensors,* vol. 9, pp. 9122-9132, 2009.

[54] J. Tu, N. Li, X. Lai, Y. Chi, Y. Zhang, W. Wang, X. Li, J. Li, and S. Qiu, "H_2S-sensing properties of Pt-doped mesoporous indium oxide," *Applied Surface Science,* vol. 256, pp. 5051-5055, 2010.

[55] M. J. Madou and S. R. Morrison, *Chemical Sensing with Solid State Devices*: Academic Press, 1989.

[56] P. Jeroschewski, K. Haase, A. Trommer, and P. Gründler, "Galvanic sensor for determination of hydrogen sulfide," *Electroanalysis,* vol. 6, pp. 769-772, 1994.

[57] Nenototech Inc. *Electrochemical Toxic Gas Sensors* [Online]. Available: http://www.nemototech.it:8080/electrochemical

[58] N. S. Lawrence, J. Davis, and R. G. Compton, "Analytical strategies for the detection of sulfide: A review," *Talanta,* vol. 52, pp. 771-784, 2000.

[59] G. Schiavon, G. Zotti, R. Toniolo, and G. Bontempelli, "Electrochemical detection of trace hydrogen sulfide in gaseous samples by porous silver electrodes supported on ion-exchange membranes (solid polymer electrolytes)," *Analytical Chemistry,* vol. 67, pp. 318-323, 1995.

[60] *Standard Test Method for Analysis of Hydrogen Sulfide in Gaseous Fuels (Lead Acetate Reaction Rate Method),* ASTM International D4084, 2007.

[61] A. Sen, J. Albarella, J. Carey, P. Kim, and W. McNamaraiii, "Low-cost colorimetric sensor for the quantitative detection of gaseous hydrogen sulfide," *Sensors and Actuators B: Chemical,* vol. 134, pp. 234-237, 2008.

[62] S. M. Sze and K. K. Ng, *Physics of Semiconductor Devices*: Wiley-Interscience, 2007.

[63] P. a. R. Brejna and P. R. Griffiths, "Electroless deposition of silver onto silicon as a method of preparation of reproducible surface-enhanced Raman spectroscopy substrates and tip-enhanced Raman spectroscopy tips," *Applied Spectrosscopy,* vol. 64, pp. 493-499, 2010.

[64] F. G. Lether and P. R. Wenston, "The numerical computation of the Voigt function by a corrected midpoint quadrature rule for $(-\infty,\infty)$," *Journal of Computational and Applied Mathematics,* vol. 34, pp. 75-92, 1991.

[65] J. J. Olivero and R. L. Longbothum, "Empirical fits to the Voigt line width: A brief review," *Journal of Quantitative Spectroscopy and Radiative Transfer,* vol. 17, pp. 233-236, 1977.

[66] J. Yang, R. C. Dennis, and D. K. Sardar, "Room-temperature synthesis of flowerlike Ag nanostructures consisting of single crystalline Ag nanoplates," *Materials Research Society Bulletin,* vol. 46, pp. 1080-1084, 2011.

[67] C. Qin and J. L. Whitten, "Interaction of S, SH and H_2S with Ag(110)," *Surface Science,* vol. 588, pp. 83-91, 2005.

[68] S. M. Russell, D. J. Liu, M. Kawai, Y. Kim, and P. A. Thiel, "Low-temperature adsorption of H_2S on Ag(111)," *Journal of Chemical Physics,* vol. 133, p. 124705, 2010.

[69] Y. C. Cao, R. Jin, and C. A. Mirkin, "Nanoparticles with Raman spectroscopic fingerprints for DNA and RNA detection," *Science,* vol. 297, pp. 1536-40, 2002.

[70] F. Bensebaa, Y. Zhou, A. G. Brolo, D. E. Irish, Y. Deslandes, E. Kruus, and T. H. Ellis, "Raman characterization of metal-alkanethiolates," *Spectrochimica Acta Part A: Molecular and Biomolecular Spectroscopy,* vol. 55, pp. 1229-1236, 1999.

[71] B. Minceva-Sukarova, M. Najdoski, I. Grozdanov, and C. J. Chunnilall, "Raman spectra of thin solid films of some metal sulfides," *Journal of Molecular Structure,* vol. 410-411, pp. 267-270, 1997.

VITA

RAMA KRISHNA RAO GOWD EDE

Candidate for the Degree of

Master of Science

Thesis: PLASMON—DAMPING CHEMICAL SENSOR FOR HYDROGEN FUEL MONITORING

Major Field: MECHANICAL AND AEROSPACE ENGINEERING

Biographical:

Education:

Completed the requirements for the Master of Science in Mechanical and Aerospace Engineering at Oklahoma State University, Stillwater, Oklahoma in December, 2011.

Completed the requirements for the Bachelor of Technology in Mechanical Engineering at Acharya Nagarjuna University, Guntur, Andhra Pradesh/India in 2005.

Name: Rama Krishna Rao Gowd Ede Date of Degree: December, 2011

Institution: Oklahoma State University Location: Stillwater, Oklahoma

Title of Study: PLASMON—DAMPING CHEMICAL SENSOR FOR HYDROGEN FUEL MONITORING

Pages in Study: 64 Candidate for the Degree of Master of Science

Major Field: Mechanical and Aerospace Engineering (MAE)

Scope and Method of Study:

Hydrogen (H_2) is a clean, sustainable, and highly energy efficient fuel source which will meet the increasing energy demand. Fuel cells can utilize H_2 and convert it into electric energy with high efficiency. However, the usage of fuel cells is limited by degradation of their performance by even trace levels of sulfur impurities (<100 ppb) present in H_2. Therefore, there is a vital need for trace level sulfur sensors to monitor the quality of H_2 fuel utilized in fuel cells. The present thesis demonstrates a novel chemical sensor using an indigenous sensing scheme: adsorbate—induced damping of hybrid plasmon resonance, associated with Ag nanoparticles, to detect ppb levels of sulfur impurities in H_2. The nanoparticles report the full width at half maximum (FWHM) or plasmon—damping factor (Γ) through optical extinction. Subsequently, H_2S concentration is calculated using time rate of change of plasmon—damping factor (i.e., $d\Delta\Gamma/dt$ or slope) in the initial linear regime.

Findings and Conclusions:

Results have shown that the change in plasmon—damping factor ($\Delta\Gamma$) related to sulfur adsorbates follows multiple Langmuir adsorption isotherms. Further, the time rate of change of plasmon—damping factor (i.e., $d\Delta\Gamma/dt$ or slope) corresponding to first Langmuir isotherm in linear regime has shown a linear response to H_2S concentration. It is also revealed that the sensitivity and response time of the present sensor is strongly dependent on $H_2S:H_2$ gas flow rate. The sensor has shown a low detection limit of 65 ppb $H_2S:H_2$, for which a response time of 10 s is observed, using a gas flow rate of 520 sccm.

ADVISER'S APPROVAL: Dr. A. Kaan Kalkan